Ultrafast imaging of coherent polariton propagation and interactions

Ding Xu¹, Arkajit Mandal¹, James M. Baxter¹, Shan-Wen Cheng¹, Inki Lee¹, Haowen Su¹, Song Liu², David R. Reichman¹, Milan Delor^{1*}

- 1. Department of Chemistry, Columbia University, New York, NY 10027, United States
- 2. Department of Mechanical Engineering, Columbia University, New York, NY 10027, United

Abstract

Semiconductor excitations can hybridize with cavity photons to form exciton-polaritons (EPs) with remarkable properties, including light-like energy flow combined with matter-like interactions. To fully harness these properties, EPs must maintain long-range coherence despite exciton-mediated interactions with lattice phonons. To address this open question, we develop a nonlinear momentum-resolved optical approach that images EPs in real space on femtosecond scales. We directly visualize EP wavepacket propagation in two-dimensional halide perovskite microcavities, allowing precise quantification of EP interactions with lattice phonons and reservoir exciton states throughout their lifetimes. We show that EP-lattice interactions strongly renormalize EP group velocities at high exciton content without sacrificing long-range coherence, enabling ballistic propagation to be maintained for up to half-exciton EPs. These results concur with our quantum simulations of dynamic disorder shielding through light-matter hybridization. We extend our measurements to molecular polaritons and self-hybridized EPs in two-dimensional materials, testifying to the remarkable generalizability of our approach.

Main text

Exciton-polaritons (EPs) form when semiconductor excitons (electron-hole pairs) hybridize with photons, resulting in renormalization of light-matter eigenstates^{1,2}. Hybridization can be readily attained with or without photonic cavities at room temperature in two-dimensional (2D), hybrid and molecular semiconductors that sustain strong light-matter interactions and large exciton binding energies³⁻⁶, paving the way to scalable polaritonic devices. EPs exhibit highly desirable properties, including photon-like coherence mediating long-range energy flow ideal for energy technologies⁷⁻¹⁰, and matter-mediated nonlinear interactions that could lead to single-photon quantum switches¹¹⁻¹⁴. The true power of EPs emerges when their light-like and matter-like features are combined; nevertheless, an open question is whether EPs can preserve long-range coherence even in the presence of strong exciton-mediated interactions with lattice phonons, other EPs, and bare excitons. Maintaining coherence in these conditions would enable EPs with high exciton content to transport extractable energy and quantum information ballistically over long distances. Simultaneously optimizing EP coherence and nonlinearities requires new approaches capable of directly tracking EP propagation and interactions with other species throughout their lifetimes.

Fast propagation and nonlinear interactions make EPs exceptionally challenging to study on their intrinsic spatiotemporal scales. Several powerful approaches have been developed to image EPs, though the majority rely on steady-state far-field optical microscopies 10,15–17 that are

unable to directly track EP propagation and nonequilibrium processes. Some ultrafast implementations of far-field microscopies have been applied to bright solitons¹⁸, condensates¹⁹ and room-temperature polaritonic systems^{20,21}, but importantly lack the momentum resolution or specie-specificity to probe EPs and their interactions with other material excitations. Recent tour-de-force experiments using ultrafast near-field scanning^{22–24} and electron²⁵ microscopies have been applied to non-cavity EPs and phonon-polaritons in van der Waals materials, boasting high momentum and spatial resolution, allowing direct tracking of polariton wavepackets on sub-picosecond scales. Nevertheless, near-field approaches are not generalizable to microcavity EPs and other complex material architectures that require sub-surface penetration, and the extension of electron microscopies to microcavity EPs and fragile materials remains untested.

Here we develop a highly generalizable and noninvasive approach based on spatiotemporally resolved far-field optical microscopy^{26,27} allowing direct imaging of EP propagation and interactions on femtosecond–nanosecond and nanometer–micrometer scales. We term our approach Momentum-resolved Ultrafast Polariton Imaging (MUPI). By directly tracking EPs and excitons throughout their lifetimes, we quantify the key factors affecting EP propagation, including EP-lattice, EP-EP and EP-exciton scattering as a function of light versus matter composition, quantities that were never directly empirically accessed. We demonstrate that our approach is generalizable across microcavity EPs, self-hybridized EPs in material slabs without external cavities, and plasmon-exciton (plexciton) polaritons in a range of emerging molecular and material systems. We focus our analysis on 2D halide perovskite microcavities at room temperature, an ideal test system that reaches the strong coupling limit without complicated cavity fabrication, possesses strong EP interactions²⁸, and displays low intrinsic exciton diffusivity^{29,30} allowing unambiguous spatial isolation of excitonic versus EP signals. We reveal that EPs in these systems are strongly affected by scattering with lattice phonons and interactions with reservoir exciton states, but remarkably retain coherent (ballistic) transport for EPs with up to 40% exciton content.

MUPI imaging of incoherent exciton and coherent EP propagation. MUPI is illustrated in Figure 1a (see Figures S1-S2 for more detail). A diffraction-limited femtosecond visible pump pulse generates excitons or EPs by exciting the material either above-gap or at a polariton resonance. A widefield backscattering probe³¹ then images the sample with and without the pump pulse at controlled time delays. Differential pump ON/pump OFF images provide a direct readout of the spatial distribution of pump-generated species, which can be tracked with sub-diffraction spatial precision^{26,27}. Momentum-matched probing of different EP modes (Figure 1b) in MUPI is achieved by displacing the probe along the optical axis of the objective, resulting in tilted widefield illumination of the sample³². The use of a high numerical aperture microscope objective (NA = 1.4) provides access to EP momenta $k = 2\pi \text{ NA}/\lambda$ greater than 10 µm⁻¹, where λ is the wavelength of light. The sample can be imaged either in real space to track exciton and EP propagation (Figures 1c-g), or in momentum-space to provide the linear and nonlinear (excited state) EP dispersion through angle-resolved reflectance spectra (Figure 1h-j).

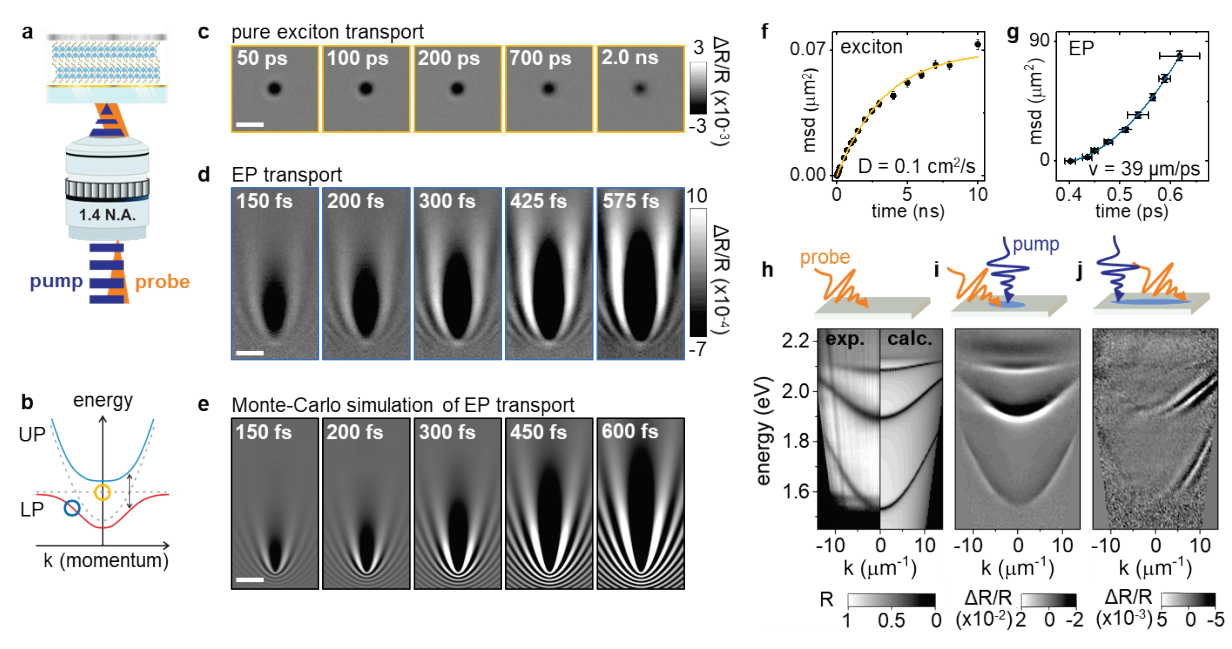


Figure 1. Tracking EPs in a layered halide perovskite microcavity. (a) MUPI setup and sample. (b) Illustration of hybridization between excitons (dashed horizontal line) and a cavity mode (dashed parabola), creating an upper polariton branch (UP) and a lower polariton branch (LP). (c) Purely excitonic transport probed at k = 0, E = 2.17 eV (the exciton resonance) following abovegap pump excitation. (d) EP transport probed at $k = 8.98 \, \mu \text{m}^{-1}$, $E = 1.77 \, \text{eV}$ (LP) following abovegap pump excitation. (e) Monte-Carlo simulation of MUPI contrast and EP propagation for the EP mode experimentally probed in panel (d). Scale bars for panels (c-e) are 2 µm. (f) Mean squared displacement (msd) of bare excitons from data in panel (c). The solid curve is a fit assuming traplimited diffusive transport. (g) msd of EPs from data in panel (d). The solid curve is a fit assuming ballistic transport. (h) Dispersion of EPs probed using angle-resolved white light reflectance. The experimental (left panel) and scattering matrix simulation (right panel) spectra agree well. (i) Differential pump ON/pump OFF angle-resolved reflectance spectrum obtained at 1 picosecond pump-probe time delay, displaying pump-induced modification to the EP dispersion when pump and probe beams are spatially overlapped. (i) Same as panel (i), with the probe spatially separated from the pump by 1.1 µm, selectively probing EP species that have propagated away from the excitation spot.

We focus our analysis on a 0.67 μ m thick slab of the layered halide perovskite (CH₃(CH₂)₃NH₃)₂(CH₃NH₃)Pb₂I₇ flanked by two metallic mirrors (Figure S3). The dispersion of our structure is shown in Figure 1h, with three resolved lower polariton (LP) branches. A fit to the experimental dispersion using a coupled oscillator model indicates a Rabi splitting of 275 meV (Figure S4), similar to previous reports²⁸. Figure 1c displays purely excitonic transport in this structure by pumping above-gap and probing at resonance with the uncoupled excitons at k=0 (orange circle in Figure 1b; see also Movie S1 and analysis in Figure S5). The exciton mean squared displacement (msd) in Figure 1f displays an exponentially-decaying msd over a few nanoseconds, characteristic of trap-limited diffusive transport³⁰. We extract a diffusivity of 0.10 \pm 0.03 cm²/s and a trap density of 29 μ m⁻². These values are in good agreement with recent reports of cavity-free exciton transport in these materials^{29,30}, indicating that the transport of bare excitons is unaffected by the cavity.

Figure 1d displays EP propagation at the same location using the same above-gap pump excitation conditions, but probing at an energy and momentum corresponding to the blue circle in Figure 1b (see also Movie S2). The MUPI image series in Figure 1d displays a fast-propagating EP signal that extends over several microns within a few hundred femtoseconds, in stark contrast to the practically static bare exciton signal of Figure 1c. The intensity of the EP signal only becomes substantial ~300 fs after non-resonant pump excitation, since the latter primarily populates excitons uncoupled to the cavity; these reservoir excitons scatter into the LP branch on timescales dictated by exciton-phonon scattering^{33,34}, leading to a delayed rise of the EP signal. The EP msd in Figure 1g is extracted by spatially tracking the EP wavefront (see analysis in Figure S6). The msd is quadratic in time (msd $\propto t^2$, or distance $\propto t$), a characteristic signature of purely ballistic transport. The EP velocity at this momentum is $39 \pm 1 \mu m/ps$, 13% of the speed of light. The distinctive interference-like features in the MUPI image profiles arise from the tilted probe plane wave interacting with the polariton population, which we successfully reproduce in Monte-Carlo simulations (Figure 1e and Supplementary Section 5).

To elucidate optical contrast generation in MUPI, we turn to transient angle-resolved spectroscopy. The excited state EP dispersion can be monitored any distance away from the excitation to probe how propagating versus non-propagating populations affect the dispersion. At the excitation spot, pump-generated excitons lead to a shift of the optical dielectric response of the perovskite semiconductor³⁵, which results in a uniform blueshift of all LP branches (Figure 1i, modeled in Supplementary Section 6). This exciton-induced dispersion modification reinforces that changes to LP spectra do not necessarily reflect EP dynamics³⁶. In contrast, the photoinduced dispersion 1.1 µm away from the excitation location and at 1 ps pump-probe time delay (Figure 1j) reflects only the EP population, since excitons are effectively immobile on this timescale. Differential signal is only observed on one side of the dispersion, confirming that only ballistic EPs (with wavevectors pointing towards the probed location) are able to propagate from the excited to the probed location. The most striking feature in the differential signal in Figure 1j is that LP branches are broadened compared to ground state branches (Supplementary Section 6). We attribute this broadening to self-energy renormalization known to arise as a result of EP-EP interactions³⁷. In our nonlinear experiment, these EP-EP interactions manifest themselves as an ensemble blockade-like effect³⁸, wherein the presence of pump-generated EPs precludes the probe from exciting the LP branch at exactly the same energies and momenta. This nonlinear interaction between pump EPs and probe EPs generates a large contrast in MUPI that we leverage to reach exceptional signal-to-noise ratios with few-minute measurements per time delay.

EPs interact with lattice phonons but remain coherent. We now turn to a detailed analysis of how EP transport is affected by interactions with lattice phonons. We probe EP propagation at six different momenta (Figure 2a) following over-bandgap excitation, all at the same location in our structure. Our key result is displayed in Figure 2b. The EP group velocity is typically assumed to correspond to the derivative of the EP dispersion, shown as solid curves for two LP branches in Figure 2b. Toward the bottom of the dispersion, where EPs are photon-like, the experimentally-observed propagation velocity (black symbols in Figure 2b) matches the expected group velocity (3% deviation for EPs that have 8% excitonic character). As we move toward more exciton-like species, we find an increasingly large deviation from the expected group velocity (40% deviation

for EPs that have 39% excitonic character). This behavior can be rationalized by EP scattering with lattice phonons, which should increase as the excitonic character of the EP increases³⁹. Nevertheless, a remarkable observation is that even EPs that are slowed by phonon interactions remain ballistic throughout their propagation length (Figure 2c). This behavior contrasts with expected quasiparticle transport behavior, where scattering leads to a transition from ballistic to superdiffusive and then diffusive transport. Instead, the observed velocity reduction without switching to diffusive behavior is reminiscent of classical wave propagation in strongly-scattering media⁴⁰, importantly indicating that long-range coherence is preserved in our systems for EPs with up to 40% exciton character.

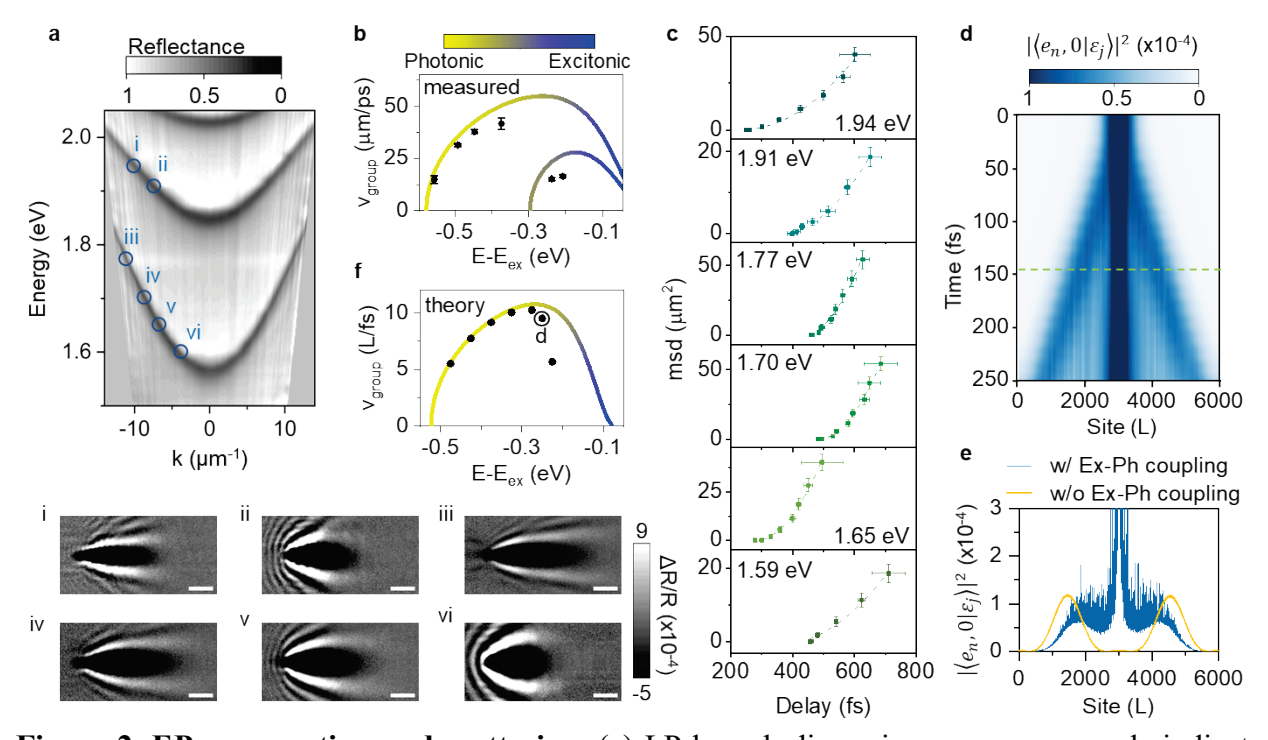


Figure 2. EP propagation and scattering. (a) LP branch dispersion; roman numerals indicate different probe momenta and energies. MUPI snapshots for each probe are displayed in the bottom panel. The pump is non-resonant (above-gap). Scale bars are 2 µm. (b) Expected group velocity (solid curve) vs. measured transport velocity (symbols) for each probing condition, showing an increasing deviation as exciton content is increased. E_{ex} corresponds to the energy of the exciton resonance. (c) EP msd for each dataset. Dashed curves are ballistic transport fits. The onset of the EP signal differs for each energy because phonon-assisted decay from the EP reservoir to the LP branch is different for each EP mode. (d) Quantum dynamical simulations of the spreading of the EP probability density $|\langle e_n, 0|\varepsilon_j\rangle|^2$ as a function of site location (L), starting with a localized initial wave-packet with an energy-window centered at $E-E_{ex}=-0.25\pm0.025$ eV. (e) EP probability density at the horizontal dashed curve cut of panel (d), for simulations with and without Holstein-type exciton-phonon coupling. (f) Computed propagation velocities from quantum dynamical simulations (symbols) compared to the group velocity obtained from the derivative of the LP branch used in our simulations (solid curve), showing comparable behavior to experimental data in panel (b).

We turn to theory to shed more light on the nature of EP-lattice interactions. Following past work on charge transport in three-dimensional halide perovskites^{41–43}, we appeal to a dynamic disorder model where transport in the absence of cavity hybridization occurs purely diffusively via the transient localization mechanism^{44,45}. The full Hamiltonian describes a single exciton coupled to phonons and an optical cavity (Supplementary Section 7). Coupling to the cavity has a dramatic effect on the transport properties of EPs⁴⁶. In particular, while the instantaneous eigenstates which govern transport of the pure exciton-phonon system exhibit significant localization, polaritonic eigenstates are largely delocalized. This qualitative change shields photon-like EPs from phonon scattering, and leads to ballistic spreading of the polariton wavepacket (Figure S12). As the EP excitonic character increases, the percentage of localized state character correspondingly increases (non-propagating states in Figure 2d). Interestingly, however, a substantial part of the EP population continues to propagate ballistically even for large exciton content (cone-like wavepacket in Figure 2d). Although ballistic propagation is preserved, the wavepacket velocity is reduced by phonon-mediated transient localization, in agreement with our experimental observations. Figure 2e compares the computed probability distributions at 145 fs for EPs with and without Holstein-type exciton-phonon coupling (setting $\gamma = 0$ in Equation S1), confirming that phonon interactions can substantially slow EP wavepackets without destroying their coherence. Figure 2f summarizes the calculated ballistic wavepacket velocities for different EPs along the simulated LP branch. The observed trend is in good agreement with the experimental behavior (Figure 2b). We therefore conclude that despite strong exciton-mediated interactions with lattice phonons, EPs at least partially retain coherent transport character throughout their propagation length even at high exciton content.

Uncoupled excitons act as reservoir states but not sinks. The above-gap pump excitation we have used thus far generates a large population of long-lived excitons that are not coupled to the cavity, often referred to as dark states 47,48. To elucidate the role that these excitons play in EP assemblies, we now compare transport behavior upon non-resonant (above-gap) excitation versus resonant excitation of the LP branch, as illustrated in Figure 3a. Figure 3b displays MUPI data when pumping above-gap and probing the LP branch up to a time delay of 1 ns; surprisingly, EPassociated signals are present 1 ns after photoexcitation, despite the EP lifetime of ~300 fs in our system. Such long lifetimes of the LP branch are regularly observed in time-resolved spectroscopy of EP assemblies^{47,49}, but recent reports cast doubt on the nature of this signal³⁶. The observed species propagates over many microns in less than a picosecond, establishing unambiguously that the signal corresponds to EPs. Indeed, the propagation itself ceases after a few hundred femtoseconds (limited by the intrinsic EP lifetime), but the signal persists and remains static from ~800 fs to 1 ns. These observations lend support to the exciton reservoir hypothesis^{47,49}, wherein uncoupled excitons populated by the non-resonant pump can scatter into the LP branch, continuously refilling the LP population throughout the exciton reservoir lifetime (1.5 ns in our case). This hypothesis is further confirmed by resonant excitation data in Figure 3c, wherein the exciton reservoir is not populated by photoexcitation. Under non-resonant excitation, we observe ballistic propagation of an EP wavepacket (highlighted with the orange circle), with the signal disappearing entirely after 800 fs. These results also suggest that backscattering from the LP branch to the exciton reservoir is negligible in our sample.

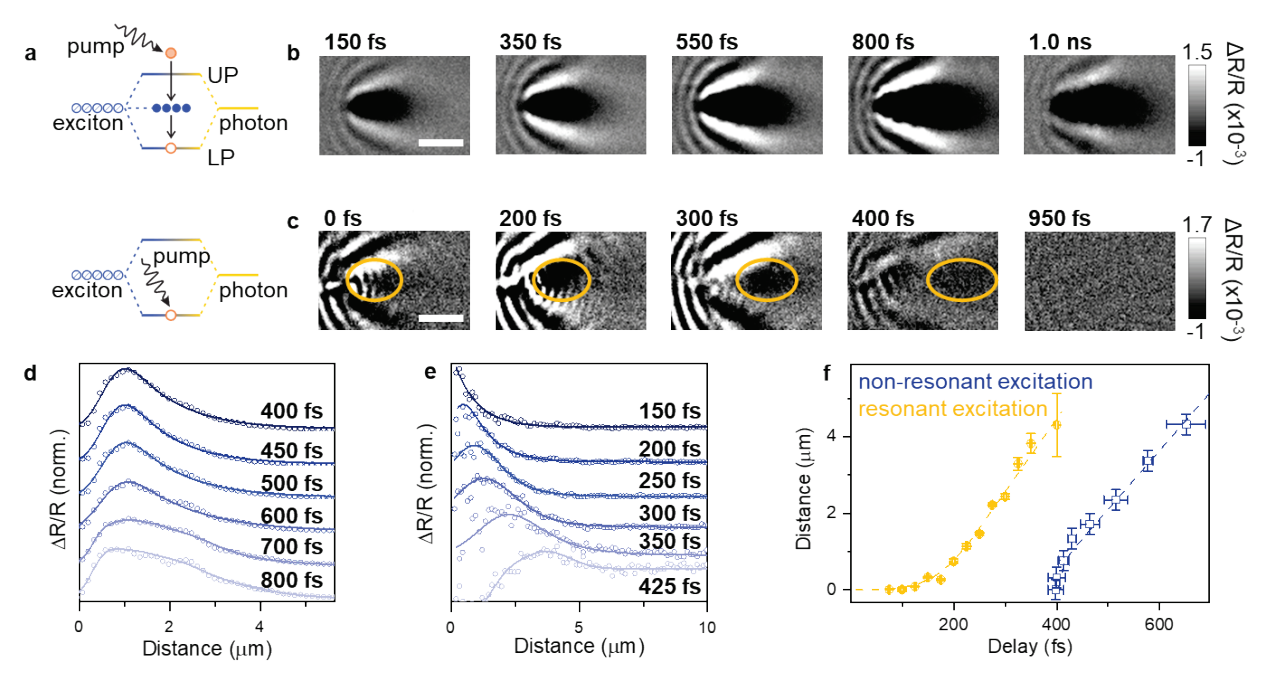


Figure 3. Resonant vs non-resonant excitation of EPs. (a) Tavis-Cummings model where hybridization between a cavity mode and N excitons leads to N-1 uncoupled excitons (blue circles, also known as dark states). The two different pump excitation conditions for panels (b) and (c) are illustrated at top and bottom, respectively. (b) Non-resonantly excited EPs probed at E = 1.91 eV and k = 6.90 µm⁻¹ (LP branch) propagate rapidly in the first ~800 fs and then remain static for a nanosecond. (c) Resonantly excited EPs with both pump and probe at E = 1.91 eV and k = 6.90 µm⁻¹ (LP branch) display a fast-propagating EP wavepacket that disappears after ~800 fs. The orange circle highlights the EP wavepacket on top of the strong scattering background; the latter is difficult to avoid in degenerate pump-probe microscopy. Scale bars are 2 µm. (d,e) Evolution of spatial profiles of EPs for non-resonant (d) and resonant (e) excitation. (f) EP transport extracted from the data in panels (d,e); see Supplementary Section 8 for detailed analysis. The dashed lines are from Monte-Carlo simulations of EP transport incorporating EP-EP scattering in the case of resonant excitation.

Figures 3d-f display the transport properties of non-resonantly vs resonantly-populated EPs (additional data and analysis are presented in Supplementary Section 8). In the long-time limit, we find that both types of EPs propagate at almost the same velocity (Figure 3f). The momentum-dependent propagation velocities for non-resonant excitation displayed in Figure 2b are commensurate for resonant excitation (Figure S14), indicating that the observed EP-lattice scattering behavior is independent of excitation condition. The early-time behavior, however, is different. For the data displayed in Figure 3, non-resonant excitation leads to slow EP population buildup reaching a maximum at ~400 fs after photoexcitation; in contrast, resonant excitation leads to full population buildup within 100 fs. In the latter case, we observe slow but accelerating initial propagation; we attribute this result to the high density of EPs at the excitation location which results in strong EP-EP scattering, slowing down the initial EP propagation. As EPs decay and propagate, the EP density decreases and EP propagation speed concomitantly increases, reaching its final transport velocity ~220 fs after excitation. We reproduce this acceleration in Monte-Carlo

simulations which take into account density-dependent EP-EP scattering (dashed lines in Figure 3f, see Supplementary Section 5 for details). These temporally inhomogeneous dynamics, similar to those recently discovered in phonon-polaritons²⁵, further emphasize the importance of tracking EPs throughout their lifetimes to characterize interactions between the many different component excitations of polaritonic systems.

Generalizability of MUPI. Finally, we show that MUPI is generalizable to many different polaritonic assemblies, though we do not perform a detailed analysis here. Along with microcavity polaritons, Figure 4 displays MUPI snapshots at 1 picosecond delay of self-hybridized (cavity-free) EPs in layered halide perovskites²⁸ and transition metal dichalcogenide (WSe₂) slabs^{23,50}, as well as coupled plasmon-excitons (plexcitons) in systems comprised of amorphous 6,13-Bis(triisopropylsilylethynyl)pentacene (TIPS-Pn) deposited on plasmonic silver thin films. We observe ballistic transport on femtosecond scales (except for plexcitons where the full propagation occurs within our instrument response), followed by static signals over more than tens of picoseconds when non-resonant excitation is used. As expected, propagation distances in self-hybridized cavities are much shorter compared to artificial cavities due to the shorter EP lifetime. Plexcitons exhibit much longer propagation lengths thanks to the highly dispersive plasmon modes imparting group velocities approaching the speed of light, despite the disordered nature of the amorphous molecular system used here.

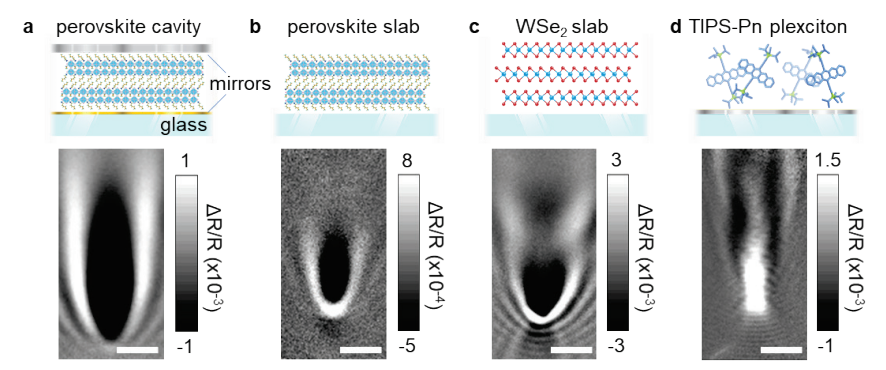


Figure 4. Generalizability of MUPI. Snapshots of MUPI at 1 ps pump-probe time delay following non-resonant excitation for: (a) EP transport in the layered halide perovskite structure used throughout the text; (b) EP transport in a 1.13 μm thick layered halide perovskite slab (CH₃(CH₂)₃NH₃)₂(CH₃NH₃)Pb₂I₇) with no artificial cavity (Figure S16a); (c) EP transport in a 69 nm thick flake of WSe₂ with no artificial cavity (Figure S16b); (d) Plexciton transport in a 30 nm Ag film/50 nm TIPS-Pn amorphous film heterostructure. Scale bars are all 2 μm.

Conclusion. We develop a momentum-selective ultrafast optical imaging approach that directly visualizes EP propagation in real space and time in a wide range of emerging semiconductors. We unambiguously demonstrate that EPs propagate ballistically over tens of microns, a characteristic of macroscopically coherent transport. We also show that the transport of uncoupled excitons is unaffected by the cavity in our structures. Even though these long-lived reservoir excitons continuously replenish the lower polariton branch throughout their lifetime, EP propagation

lengths remain limited by the intrinsic EP lifetime. We find that the group velocities of EPs with large excitonic character are substantially reduced through scattering with lattice phonons; remarkably, however, EPs maintain a high degree of coherence and thus long-range ballistic transport even in these strongly-interacting environments. Quantum dynamical simulations indicate that this behavior arises from the interplay of transient localization of EPs induced by strong exciton-phonon interactions and partial shielding of these interactions by hybridization with the cavity. These unique properties firmly establish EPs as ideal information carriers for quantum technologies that rely on nonlinear interactions of wavelike particles.

Acknowledgements

This material is based upon work supported by the National Science Foundation under Grant No. DMR-2115625. A.M. and D.R.R. acknowledge the National Science Foundation for funding through grant CHE-1954791. Synthesis of WSe₂ (S.L.) was supported by the NSF MRSEC program through Columbia in the Center for Precision-Assembled Quantum Materials (DMR-2011738). This work used the Extreme Science and Engineering Discovery Environment (XSEDE), which is supported by National Science Foundation grant number ACI-1548562 (allocations: TG-CHE210085). Specifically, it used the services provided by the OSG Consortium, which is supported by the National Science Foundation awards #2030508 and #1836650.

Author contributions

D.X. and M.D. conceived and designed the experiments. D.X. and J.B. developed the instrument. D.X, S.C., I.L. and H.S. acquired the experimental data. S.L. synthesized WSe₂ crystals. D.X. analyzed the data. A.M. and D.R.R. carried out the quantum dynamical simulations. D.X., A.M., D.R.R. and M.D. wrote the manuscript, with input from all authors.

Competing interests

The authors declare no competing interests

Additional Information

Correspondence and requests for materials should be addressed to Milan Delor (milan.delor@columbia.edu)

References

- 1. Mills, D. L. & Burstein, E. Polaritons: the electromagnetic modes of media. *Reports Prog. Phys.* **37**, 817–926 (1974).
- 2. Weisbuch, C., Nishioka, M., Ishikawa, A. & Arakawa, Y. Observation of the coupled exciton-photon mode splitting in a semiconductor quantum microcavity. *Phys. Rev. Lett.* **69**, 3314–3317 (1992).
- 3. Basov, D. N., Fogler, M. M. & García de Abajo, F. J. Polaritons in van der Waals materials. *Science* **354**, 195 (2016).
- 4. Liu, X. et al. Strong light-matter coupling in two-dimensional atomic crystals. Nat.

- Photonics 9, 30–34 (2015).
- 5. Sanvitto, D. & Kéna-Cohen, S. The road towards polaritonic devices. *Nat. Mater.* **15**, 1061–1073 (2016).
- 6. Su, R. *et al.* Perovskite semiconductors for room-temperature exciton-polaritonics. *Nat. Mater.* **20**, 1315–1324 (2021).
- 7. Steger, M. *et al.* Long-range ballistic motion and coherent flow of long-lifetime polaritons. *Phys. Rev. B* **88**, 235314 (2013).
- 8. Coles, D. M. *et al.* Polariton-mediated energy transfer between organic dyes in a strongly coupled optical microcavity. *Nat. Mater.* **13**, 712–719 (2014).
- 9. Orgiu, E. *et al.* Conductivity in organic semiconductors hybridized with the vacuum field. *Nat. Mater.* **14**, 1123–1129 (2015).
- 10. Hou, S. *et al.* Ultralong-Range Energy Transport in a Disordered Organic Semiconductor at Room Temperature Via Coherent Exciton-Polariton Propagation. *Adv. Mater.* **32**, 2002127 (2020).
- 11. Delteil, A. *et al.* Towards polariton blockade of confined exciton–polaritons. *Nat. Mater.* **18**, 219–222 (2019).
- 12. Muñoz-Matutano, G. *et al.* Emergence of quantum correlations from interacting fibre-cavity polaritons. *Nat. Mater.* **18**, 213–218 (2019).
- 13. Cuevas, Á. *et al.* First observation of the quantized exciton-polariton field and effect of interactions on a single polariton. *Sci. Adv.* 4, eaao6814 (2018).
- 14. Zasedatelev, A. V. *et al.* Single-photon nonlinearity at room temperature. *Nature* **597**, 493–497 (2021).
- 15. Lerario, G. *et al.* High-speed flow of interacting organic polaritons. *Light Sci. Appl.* **6**, e16212-6 (2017).
- 16. Wurdack, M. *et al.* Motional narrowing, ballistic transport, and trapping of room-temperature exciton polaritons in an atomically-thin semiconductor. *Nat. Commun.* **12**, 5366 (2021).
- 17. Myers, D. M. et al. Polariton-enhanced exciton transport. Phys. Rev. B 98, 235302 (2018).
- 18. Sich, M. *et al.* Observation of bright polariton solitons in a semiconductor microcavity. *Nat. Photonics* **6**, 50–55 (2012).
- 19. Gianfrate, A. *et al.* Superluminal X-waves in a polariton quantum fluid. *Light Sci. Appl.* 7, 17119–17119 (2018).
- 20. Pandya, R. *et al.* Microcavity-like exciton-polaritons can be the primary photoexcitation in bare organic semiconductors. *Nat. Commun.* **12**, 6519 (2021).
- 21. Rozenman, G. G., Akulov, K., Golombek, A. & Schwartz, T. Long-Range Transport of Organic Exciton-Polaritons Revealed by Ultrafast Microscopy. *ACS Photonics* **5**, 105–110 (2018).

- 22. Yoxall, E. *et al.* Direct observation of ultraslow hyperbolic polariton propagation with negative phase velocity. *Nat. Photonics* **9**, 674–678 (2015).
- 23. Mrejen, M., Yadgarov, L., Levanon, A. & Suchowski, H. Transient exciton-polariton dynamics in WSe 2 by ultrafast near-field imaging. *Sci. Adv.* 5, eaat9618 (2019).
- 24. Huber, M. A. *et al.* Femtosecond photo-switching of interface polaritons in black phosphorus heterostructures. *Nat. Nanotechnol.* **12**, 207–211 (2017).
- 25. Kurman, Y. *et al.* Spatiotemporal imaging of 2D polariton wave packet dynamics using free electrons. *Science* **372**, 1181–1186 (2021).
- 26. Zhu, T., Snaider, J. M., Yuan, L. & Huang, L. Ultrafast Dynamic Microscopy of Carrier and Exciton Transport. *Annu. Rev. Phys. Chem.* **70**, 219–244 (2019).
- 27. Ginsberg, N. S. & Tisdale, W. A. Spatially Resolved Exciton and Charge Transport in Emerging Semiconductors. *Annu. Rev. Phys. Chem.* **71**, 1–30 (2020).
- 28. Fieramosca, A. *et al.* Two-dimensional hybrid perovskites sustaining strong polariton interactions at room temperature. *Sci. Adv.* 5, eaav9967 (2019).
- 29. Deng, S. *et al.* Long-range exciton transport and slow annihilation in two-dimensional hybrid perovskites. *Nat. Commun.* **11**, 664 (2020).
- 30. Seitz, M. *et al.* Exciton diffusion in two-dimensional metal-halide perovskites. *Nat. Commun.* **11**, 2035 (2020).
- 31. Delor, M., Weaver, H. L., Yu, Q. & Ginsberg, N. S. Imaging material functionality through three-dimensional nanoscale tracking of energy flow. *Nat. Mater.* **19**, 56–62 (2020).
- 32. Huang, B., Yu, F. & Zare, R. N. Surface plasmon resonance imaging using a high numerical aperture microscope objective. *Anal. Chem.* **79**, 2979–2983 (2007).
- 33. Imamoglu, A., Ram, R. J., Pau, S. & Yamamoto, Y. Nonequilibrium condensates and lasers without inversion: Exciton-polariton lasers. *Phys. Rev. A* **53**, 4250–4253 (1996).
- 34. Somaschi, N. *et al.* Ultrafast polariton population build-up mediated by molecular phonons in organic microcavities. *Appl. Phys. Lett.* **99**, 143303 (2011).
- 35. Wu, X., Trinh, M. T. & Zhu, X. Y. Excitonic Many-Body Interactions in Two-Dimensional Lead Iodide Perovskite Quantum Wells. *J. Phys. Chem. C* **119**, 14714–14721 (2015).
- 36. Renken, S. *et al.* Untargeted effects in organic exciton–polariton transient spectroscopy: A cautionary tale. *J. Chem. Phys.* **155**, 154701 (2021).
- 37. Sun, Y. *et al.* Direct measurement of polariton–polariton interaction strength. *Nat. Phys.* **13**, 870–875 (2017).
- 38. Verger, A., Ciuti, C. & Carusotto, I. Polariton quantum blockade in a photonic dot. *Phys. Rev. B* **73**, 193306 (2006).
- 39. Hopfield, J. J. Resonant Scattering of Polaritons as Composite Particles. *Phys. Rev.* **182**, 945 (1969).

- 40. Page, J. H. et al. Group Velocity in Strongly Scattering Media. Science 271, 634–637 (1996).
- 41. Mayers, M. Z., Tan, L. Z., Egger, D. A., Rappe, A. M. & Reichman, D. R. How Lattice and Charge Fluctuations Control Carrier Dynamics in Halide Perovskites. *Nano Lett.* **18**, 8041–8046 (2018).
- 42. Schilcher, M. J. *et al.* The Significance of Polarons and Dynamic Disorder in Halide Perovskites. *ACS Energy Lett.* **6**, 2162–2173 (2021).
- 43. Lacroix, A., de Laissardière, G. T., Quémerais, P., Julien, J.-P. & Mayou, D. Modeling of Electronic Mobilities in Halide Perovskites: Adiabatic Quantum Localization Scenario. *Phys. Rev. Lett.* **124**, 196601 (2020).
- 44. Fratini, S., Mayou, D. & Ciuchi, S. The Transient Localization Scenario for Charge Transport in Crystalline Organic Materials. *Adv. Funct. Mater.* **26**, 2292–2315 (2016).
- 45. Troisi, A. & Orlandi, G. Charge-Transport Regime of Crystalline Organic Semiconductors: Diffusion Limited by Thermal Off-Diagonal Electronic Disorder. *Phys. Rev. Lett.* **96**, 086601 (2006).
- 46. Ferreira, B., Rosati, R. & Malic, E. Microscopic modeling of exciton-polariton diffusion coefficients in atomically thin semiconductors. *Phys. Rev. Mater.* **6**, 034008 (2022).
- 47. Ebbesen, T. W. Hybrid Light-Matter States in a Molecular and Material Science Perspective. *Acc. Chem. Res.* **49**, 2403–2412 (2016).
- 48. Ribeiro, R. F., Martínez-Martínez, L. A., Du, M., Campos-Gonzalez-Angulo, J. & Yuen-Zhou, J. Polariton chemistry: controlling molecular dynamics with optical cavities. *Chem. Sci.* **9**, 6325–6339 (2018).
- 49. Virgili, T. *et al.* Ultrafast polariton relaxation dynamics in an organic semiconductor microcavity. *Phys. Rev. B* **83**, 245309 (2011).
- 50. Hu, F. *et al.* Imaging exciton–polariton transport in MoSe₂ waveguides. *Nat. Photonics* **11**, 356–360 (2017).

Supplementary information for

Ultrafast imaging of coherent polariton propagation and interactions

Ding Xu¹, Arkajit Mandal¹, James M. Baxter¹, Shan-Wen Cheng¹, Inki Lee¹, Haowen Su¹, Song Liu², David R. Reichman¹, and Milan Delor^{1*}

- 1. Department of Chemistry, Columbia University, New York, NY 10027, United States
- 2. Department of Mechanical Engineering, Columbia University, New York, NY 10027, United States

1. Sample preparation

CH₃(CH₂)₃NH₃)₂(CH₃NH₃)Pb₂I₇ (BA₂(MA)Pb₂I₇) crystal synthesis. Ruddlesden-Popper perovskites (RPP)¹ have a general formula, $A_2A'_{n-1}M_nX_{3n+1}$, where A and A' are cations, M is a metal, X is a halide, and n is the perovskite layer thickness. The preparation of EP cavities for MUPI measurements requires exfoliating large-area high-quality flakes of uniform thickness, which we could achieve for n = 1 and n = 2 flakes but was more challenging for n > 2 RPP perovskites. We focus the text on n = 2 flakes (BA₂(MA)Pb₂I₇). All chemicals were purchased from Sigma-Aldrich. The synthesis followed a published procedure. Hydriodic acid (HI) solution was prepared by mixing 57% wt. aqueous HI (9 mL) and 50% wt. aqueous Hypophosphorous acid (H₃PO₂, 1 mL). Lead (II) iodide (PbI₂, 99.999% trace metals bases) powder (2720 mg, 5.9 mmol) was dissolved in the mixture solution under constant magnetic stirring. Methylammonium iodide (MAI, ≥ 99%, anhydrous 493 mg, 3.1 mmol) was added to the solution and black powder precipitated instantly. The black powder redissolved quickly by heating the solution to 100 °C with stirring. Subsequent addition of n-Butylammonium iodide (BAI, 864 mg, 4.3 mmol) caused the crystallization of bright orange flakes on the top of the solution. The solution was heated up to 105 °C under constant magnetic stirring until all precipitation dissolved. The solution was subjected to controlled cooling rate of 0.5 °C/h to room temperature in an oil bath, and large crystals formed on the solution surface. The crystals were collected by vacuum filtering and washed twice with toluene.

Artificial cavity fabrication. The bottom partial reflector through which light impinges the sample is a 30 nm gold film that was deposited on cover glass (Richard-Allan Scientific, 24×50 #1.5) by e-beam evaporation (Angstrom EvoVac deposition system). The deposition rate was 0.05 nm/s. The perovskites flakes were then mechanically exfoliated onto the gold-deposited cover glass with PVC tape (Nitto SPV224 PVC Vinyl Surface Protection Specialty Tape). Although gold is more lossy compared to silver, thin (<50 nm) silver films tend to deteriorate during measurements, which rapidly leads to poor imaging quality, an important aspect for our scattering-based experiments. The top reflector is a 200 nm silver film that was prepared by e-beam deposition on a silicon wafer. A layer of polyvinylpyrrolidone (PVP) solution (Sigma Aldrich, M.W. 40000, 10% wt in ethanol/acetonitrile wt 1/1) was then spin-coated on the silver film (3000 rpm, acceleration 1000rpm/s, 2min) and thermally annealed at 150 °C for 5 min. The prepared PVP/Ag was picked up with thermal release tape (semiconductor corp., release temperature 90 °C) and placed on the perovskites flakes with firm pressure, completing the cavity structure. The full structures were encapsulated between glass slides using epoxy (OG159-2, Epoxy Technology) in a nitrogen-filled glovebox to prevent sample oxidation during the measurements.

WSe₂ sample preparation. The self-hybridized WSe₂ cavity sample was prepared by direct Scotch-tape mechanical exfoliation of bulk high-purity flux-grown WSe₂ crystals^{3,4} onto a borosilicate cover glass. Flakes of the right thickness were found using atomic force microscopy (Bruker Dimension FastScan Atomic Force Microscope).

6,13-Bis(triisopropylsilylethynyl)pentacene (TIPS-pentacene) plexciton sample preparation. A 30 nm silver film was deposited on cover glass by e-beam deposition (at 0.05 nm/s), creating a plasmonic film. The silver is then coated with a 3 nm Al_2O_3 top layer that acts to both protect the silver and prevent direct charge-transfer interactions with molecules. Al_2O_3 that was grown by atomic layer deposition (SAVANNAH 200, Cambridge Nano Tech Inc.). TIPS-Pentacene (\geq 99%, 20 mg) and poly(methyl methacrylate) (PMMA, M.W. 35000, 6 mg) was dissolved in toluene (1 mL) under constant stirring. The TIPS-pentacene/PMMA solution is then spin-coated on the silver-coated cover glass at 3000 rpm for 60 seconds.

2. Optical measurements: Momentum-resolved Ultrafast Polariton Imaging

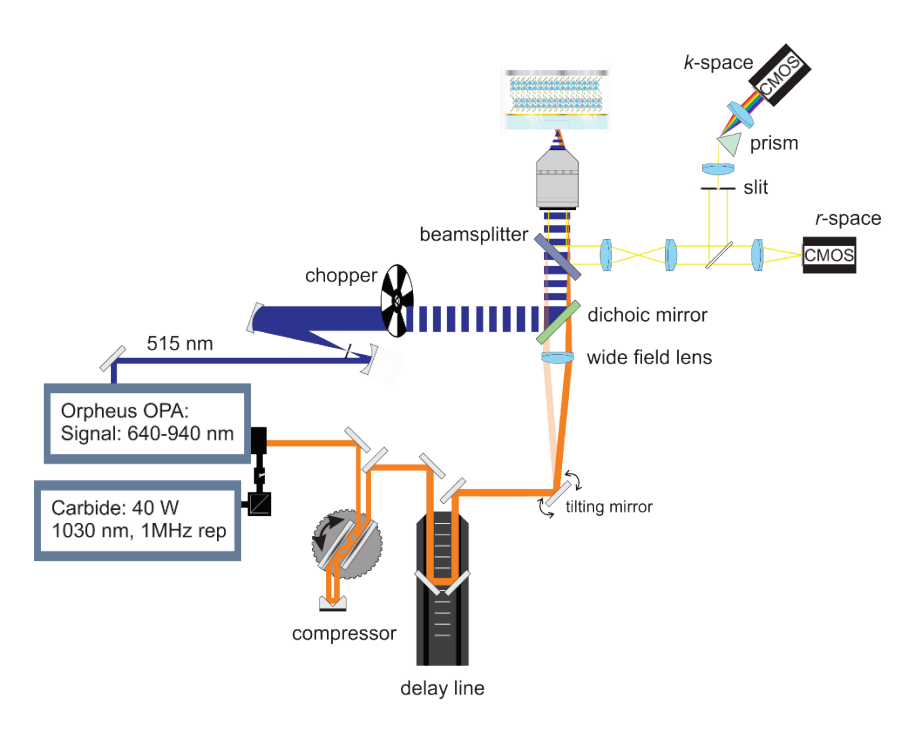


Figure S1. Optical schematic for momentum-resolved ultrafast polariton imaging.

MUPI is shown in Figure S1. A 40 W Yb:KGW ultrafast regenerative amplifier (Light Conversion Carbide, 40W, 1030 nm fundamental, 1 MHz repetition rate) seeds an optical parametric amplifier (OPA, Light Conversion, Orpheus-F) with a signal tuning range of 640 – 940 nm and an average pulsewidth of 60 fs. For non-resonant excitation experiments, the second harmonic of the fundamental (515 nm) is used as a pump pulse, and the OPA signal is used as probe. For resonant excitation (single-color) experiments, the OPA signal is split in pump and probe beams using a beamsplitter. Dispersion of the OPA signal caused by refractive optics (in particular the microscope objective) is partially pre-compensated using a pair of chirped mirrors (Venteon DCM7). For all experimental configurations, the pump pulse train is modulated at 647 Hz using an optical chopper and is sent collimated into a high numerical-aperture objective (Leica HC Plan Apo 63x, 1.4 NA oil immersion), resulting in diffraction-limited excitation on the sample. Typical pump fluence incident on the semiconductor is 5 µJ/cm². The probe is sent to a computercontrolled mechanical delay line for control over pump-probe time delay, and is combined with the pump beam through a dichroic mirror. An f = 250 mm widefield lens is inserted prior to the dichroic mirror to focus the probe in the back focal plane of the objective, resulting in widefield illumination of the sample. A tilting mirror placed one focal length upstream of the widefield lens allows tuning the angle at which the widefield probe illuminates the sample, thus allowing probing at any momentum up to a maximum of $k/k_0 = 1.4$, limited by the numerical aperture of the objective.

A beamsplitter collects the backscattered light from the sample through the objective, directing the light to two different detection paths. For angle-resolved linear and transient reflectance (Figure 1 h-j of the main text), the back focal plane of the objective is projected on the entrance slit of a

home-built prism spectrometer using a pair of lenses ($f_1 = 300$ mm and $f_2 = 100$ mm), as depicted in Figure S1. For real-space MUPI imaging, this projected back focal plane image is Fourier transformed again into real-space using a 150 mm lens, forming an image on a CMOS camera (Blackfly S USB3, BFS-U3-28S5M-C). Both the spectrometer camera and the real-space camera are triggered at double the pump modulation rate, allowing the consecutive acquisition of images with the pump ON followed by the pump OFF. Consecutive frames are then processed according to (pump on/pump off -1).

The configuration used for ultrafast angle-resolved transient reflectance experiments (Figure 1i,j) is almost identical to that described above, except that the probe is a supercontinuum white light generated by focusing the fundamental 1030 nm beam from the regenerative amplifier in a 5.0 mm yttrium aluminum garnet flat window (YAG, undoped, orientation[111], EKSMA Optics). For this experiment, the probe is sent collimated into the objective and overfills the back aperture of the objective. This configuration ensures that all angles allowed by the numerical aperture of the objective are collected, allowing the data in Figures 1i,j to be collected in a single pump/probe image pair, i.e. without having to scan across angles.

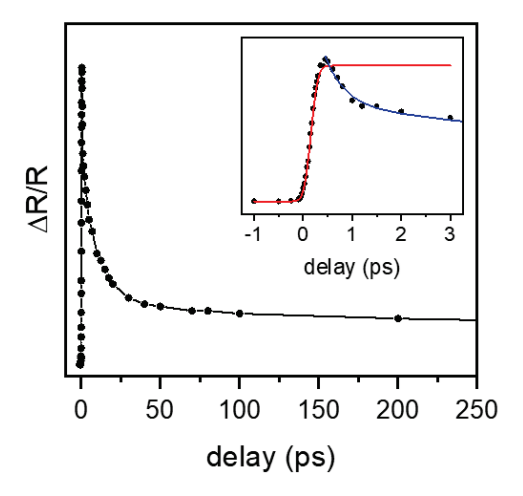


Figure S2. Normal incident pump-probe experiment using a 515 nm pump and 730 nm probe. The inset shows the early pump-probe time delay signal. The estimated instrument response function from the fit is 162 fs.

3. Sample characterization

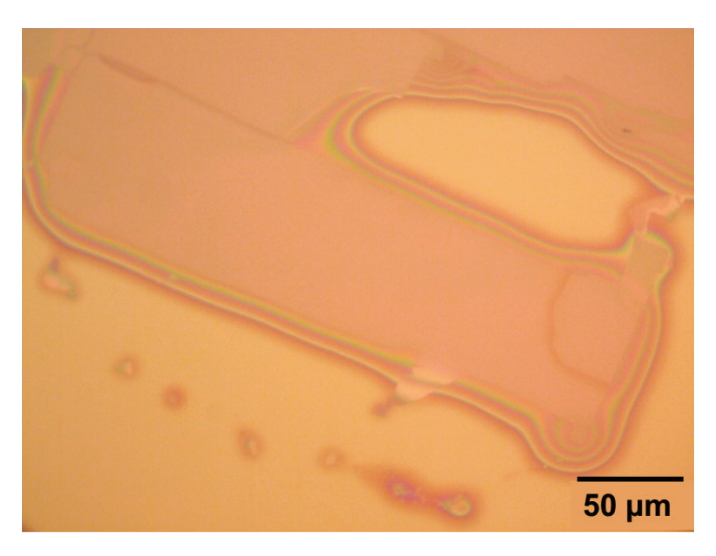


Figure S3. Example image for a $0.667~\mu m$ thick $BA_2(MA)Pb_2I_7$ single crystal flake enclosed in a Au-Ag cavity. This image was collected in reflection using a halogen white light lamp and a 40X objective. The scale bar is $50~\mu m$.

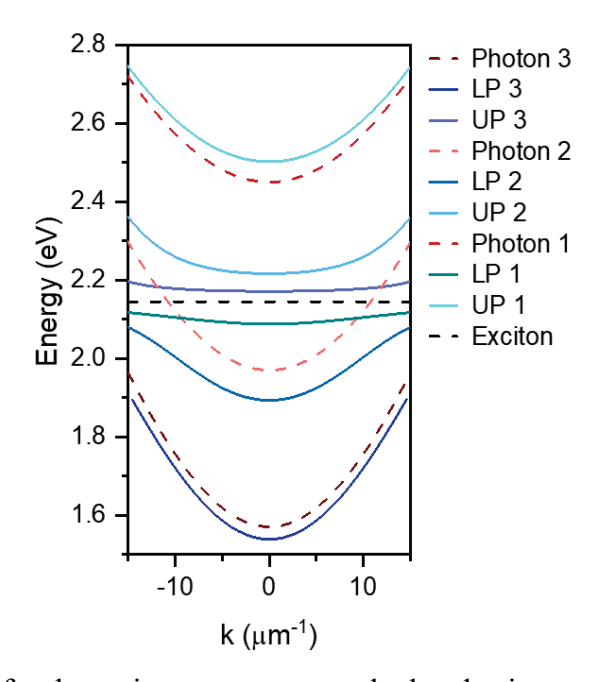


Figure S4. EP dispersion for the main text structure calculated using a coupled oscillator model.

We extract the Rabi splitting and photon/exciton content at each energy of lower polariton branches using a simple coupled oscillator model, described as^{5,6}:

$$i\hbar \frac{\partial}{\partial t} \varphi = H\varphi + \delta \chi$$

$$i\hbar \frac{\partial}{\partial t} \chi = U_{ex} \chi + \delta \varphi$$

Where the cavity photon field is φ , and the exciton field is χ . $U_{\rm ex}$ is the exciton energy, which is 2.14 eV for all momenta accessible with our objective, and H is the Hamiltonian for the uncoupled cavity photon. The photon-exciton coupling strength δ (half the Rabi splitting) is fitted as 137.5 meV. The coupled equation can be numerically solved to retrieve the polariton eigenvalue $E_{\rm pol}$ and eigenstate ϕ .

$$\begin{pmatrix} H & \delta \\ \delta & U_{ax} \end{pmatrix} \begin{pmatrix} \varphi \\ \chi \end{pmatrix} = E_{pol} \begin{pmatrix} \varphi \\ \chi \end{pmatrix}$$

The exciton content of the polariton is obtained by the eigenstate normalization:

$$\phi_{LP} = A\varphi - X\chi$$

$$\phi_{UP} = A\varphi + X\chi$$

$$|A|^2 + |X|^2 = 1$$

Where A and X are the Hopfield coefficients associated with the relative photon and exciton content of the polariton. The EP lifetime is then calculated with the exciton content:

$$\tau^{-1} = \frac{|X|^2}{\tau_{ex}} + \frac{1 - |X|^2}{\tau_{loss}}$$

$$\tau_{loss} = \frac{2nL}{1 - R_{top}R_{bottom}}$$

Where τ_{ex} is the exciton lifetime and τ_{loss} is the cavity photon loss time. The photon loss time depends on the cavity thickness L, gain medium refractive index n, and the reflection coefficients R for the top and bottom interfaces of the cavity.

The theoretical group velocity v_g of the polariton is calculated by first-order differentiation of the dispersion relation:

$$v_g = \frac{\partial \omega}{\partial k}$$

Where ω is the resonance frequency of the polariton and k is the momentum.

4. Exciton and EP transport analysis

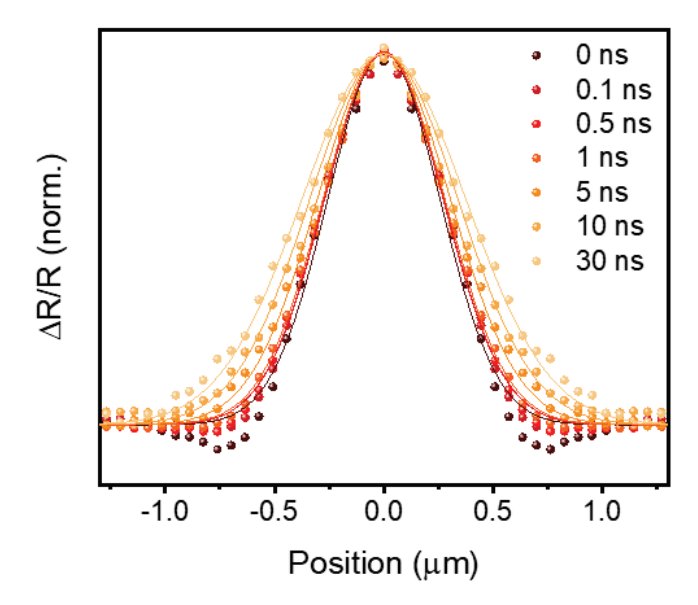


Figure S5. Bare exciton transport in BA₂(MA)Pb₂I₇ taken with a probe at the exciton resonance at k=0. The population profiles were obtained through radial averaging of the data shown in Figure 1c of the main text. Gaussian fits to the population profiles allow extracting a Gaussian width σ . The exciton mean squared displacement plotted in Figure 1f of the main text is then defined as msd = $\sigma^2(t) - \sigma^2(0) = 2Dt$, where t is the pump-probe time delay, and D is the diffusivity. Normal diffusive transport shows a linear msd in time^{7,8}. In our 2D halide perovskites, exciton transport is observed to be subdiffusive, and is fit to a trap-limited, exponentially-decaying diffusivity in agreement with recent reports⁹, as detailed in the main text. The pump fluence for this dataset is 4.44 μ J/cm².

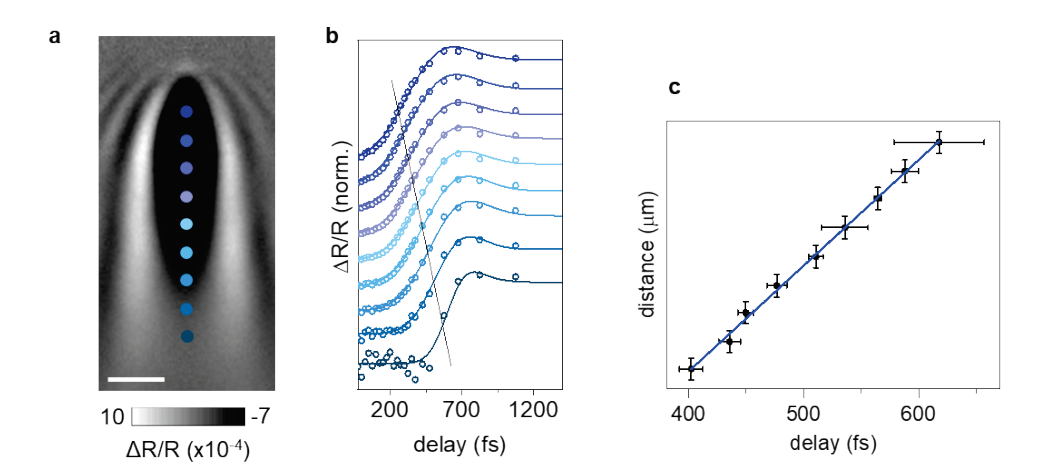


Figure S6. Example of propagation fitting for MUPI imaging of EP transport. Here, EPs are generated at the top of the image (a), and propagate downward. The signal rise-time for each location indicated by the blue dots in the image is extracted (panel b). Since the rise time at each location is a convolution of the instrument response function with the delayed arrival of the EP, the rise times are fit using a Gaussian function convolved with a bi-exponential decay (the second decay is a nanosecond decay component to account for the offset),

$$\frac{\Delta R}{R} = A_1 e^{-\frac{t}{\tau_1} + \frac{t_0 + w^2}{2\tau_1^2}} \left(1 + \operatorname{erf}\left(\frac{t - t_0 - \frac{w^2}{\tau_1}}{\sqrt{2}w}\right) \right) + A_2 e^{-\frac{t}{\tau_2} + \frac{t_0 + w^2}{2\tau_2^2}} \left(1 + \operatorname{erf}\left(\frac{t - t_0 - \frac{w^2}{\tau_2}}{\sqrt{2}w}\right) \right) + C e^{-\frac{t}{\tau_1} + \frac{t_0 + w^2}{2\tau_2^2}} \left(1 + \operatorname{erf}\left(\frac{t - t_0 - \frac{w^2}{\tau_2}}{\sqrt{2}w}\right) \right) + C e^{-\frac{t}{\tau_1} + \frac{t_0 + w^2}{2\tau_2^2}} \left(1 + \operatorname{erf}\left(\frac{t - t_0 - \frac{w^2}{\tau_2}}{\sqrt{2}w}\right) \right) + C e^{-\frac{t}{\tau_1} + \frac{t_0 + w^2}{2\tau_2^2}} \left(1 + \operatorname{erf}\left(\frac{t - t_0 - \frac{w^2}{\tau_2}}{\sqrt{2}w}\right) \right) + C e^{-\frac{t}{\tau_1} + \frac{t_0 + w^2}{2\tau_2^2}} \left(1 + \operatorname{erf}\left(\frac{t - t_0 - \frac{w^2}{\tau_2}}{\sqrt{2}w}\right) \right) + C e^{-\frac{t}{\tau_1} + \frac{t_0 + w^2}{2\tau_2^2}} \left(1 + \operatorname{erf}\left(\frac{t - t_0 - \frac{w^2}{\tau_2}}{\sqrt{2}w}\right) \right) + C e^{-\frac{t}{\tau_1} + \frac{t_0 + w^2}{2\tau_2^2}} \left(1 + \operatorname{erf}\left(\frac{t - t_0 - \frac{w^2}{\tau_2}}{\sqrt{2}w}\right) \right) + C e^{-\frac{t}{\tau_1} + \frac{t_0 + w^2}{2\tau_2^2}} \left(1 + \operatorname{erf}\left(\frac{t - t_0 - \frac{w^2}{\tau_2}}{\sqrt{2}w}\right) \right) + C e^{-\frac{t}{\tau_1} + \frac{t_0 + w^2}{2\tau_2^2}} \left(1 + \operatorname{erf}\left(\frac{t - t_0 - \frac{w^2}{\tau_2}}{\sqrt{2}w}\right) \right) + C e^{-\frac{t}{\tau_1} + \frac{t_0 + w^2}{2\tau_1^2}} \left(1 + \operatorname{erf}\left(\frac{t - t_0 - \frac{w^2}{\tau_1}}{\sqrt{2}w}\right) \right) + C e^{-\frac{t}{\tau_1} + \frac{t_0 + w^2}{2\tau_1^2}} \left(1 + \operatorname{erf}\left(\frac{t - t_0 - \frac{w^2}{\tau_1}}{\sqrt{2}w}\right) \right) + C e^{-\frac{t}{\tau_1} + \frac{t_0 + w^2}{2\tau_1^2}} \left(1 + \operatorname{erf}\left(\frac{t - t_0 - \frac{w^2}{\tau_1}}{\sqrt{2}w}\right) \right) + C e^{-\frac{t}{\tau_1} + \frac{t_0 + w^2}{2\tau_1^2}} \left(1 + \operatorname{erf}\left(\frac{t - t_0 - \frac{w^2}{\tau_1}}{\sqrt{2}w}\right) \right) + C e^{-\frac{t}{\tau_1} + \frac{t_0 + w^2}{2\tau_1^2}} \left(1 + \operatorname{erf}\left(\frac{t - t_0 - \frac{w^2}{\tau_1}}{\sqrt{2}w}\right) \right) + C e^{-\frac{t}{\tau_1} + \frac{t_0 + w^2}{2\tau_1^2}} \left(1 + \operatorname{erf}\left(\frac{t - t_0 - \frac{w^2}{\tau_1}}{\sqrt{2}w}\right) \right) + C e^{-\frac{t}{\tau_1} + \frac{t_0 + w^2}{2\tau_1^2}} \left(1 + \operatorname{erf}\left(\frac{t - t_0 - \frac{w^2}{\tau_1}}{\sqrt{2}w}\right) \right) + C e^{-\frac{t}{\tau_1} + \frac{t_0 + w^2}{2\tau_1^2}} \left(1 + \operatorname{erf}\left(\frac{t - t_0 - \frac{w^2}{\tau_1}}{\sqrt{2}w}\right) \right) + C e^{-\frac{t}{\tau_1} + \frac{t_0 + w^2}{2\tau_1^2}} \left(1 + \operatorname{erf}\left(\frac{t - t_0 - \frac{w^2}{\tau_1}}{\sqrt{2}w}\right) \right) + C e^{-\frac{t}{\tau_1} + \frac{t_0 + w^2}{2\tau_1^2}} \left(1 + \operatorname{erf}\left(\frac{t - t_0 - \frac{w^2}{\tau_1}}{\sqrt{2}w}\right) \right) + C e^{-\frac{t}{\tau_1} + \frac{t_0 + w^2}{2\tau_1^2}} \left(1 + \operatorname{erf}\left(\frac{t - t_0 - \frac{w^2}{\tau_1}}{\sqrt{2}w}\right) \right) + C e^{-\frac{t}{\tau_1} + \frac{w^2}{\tau_1}} \left(1 + \operatorname{erf}\left(\frac{t - t_$$

where A_1 , A_2 , τ_1 , τ_2 are fit amplitudes and decay times, w is the instrument response function width, and t_0 is defined as the EP arrival time. Additional fits and datasets are provided in Figure S13. Note that this fitting procedure provides almost identical results to extracting the EP arrival time as the time at which the EP signal rises to half its maximum amplitude (schematically illustrated with the black line in panel b). (c) Resulting distance vs delay plot extracted from the fitting procedure, showing linear behavior. Note that the msd (rather than distance) is plotted in the main text.

5. Monte-Carlo simulations of polariton transport

To model the imaging patterns observed in MUPI, Monte-Carlo simulations such as that shown in Figure 1e of the main text were carried out. In these simulations, imaged EP 'particles' are assumed to move ballistically at the group velocity extracted from the polariton dispersion, and along the wavevector probed by the probe field, until they are elastically scattered by the lattice. For non-resonant excitation, the EP injection rate is modeled according to the empirical rise-time of the signal; this finite rise-time reflects population scattering from the long-lived exciton reservoir to the lower polariton branch (Figure S7). For resonant excitation, the EP injection rate is modeled after the instrument response function (Figure S2). In the Monte-Carlo model, the EP particles are initialized having the same group velocity, and with a spatial Gaussian distribution

$$G(r,\sigma) = \frac{1}{\sqrt{2\pi\sigma}} \exp(-\frac{r^2}{2\sigma^2})$$

where r is the distance of the EPs to the excitation origin and σ is the standard deviation of the distribution, which is set to be the diffraction limit for the pump wavelength used. The directions of EPs moving angle are randomized in the initialization. At each time step of dt = 10 fs, we calculate the probability of EP-lattice scattering and EP loss with $\exp(-\text{dt}/\tau_{phonon})$ and $\exp(-\text{dt}/\tau_{life})$, τ_{phonon} and τ_{life} are the EP-lattice scattering time and polariton lifetime, respectively. In these simulations, τ_{phonon} is empirically tuned to match the transport behavior observed in our experiments. The elastically scattered EPs are then assigned a new random angle (Figure S8a). To reproduce MUPI images, wherein the probe selects only EPs with specific wavevectors, we selectively plotted EPs populated within a finite range of angles corresponding to the probe momentum for further processing, even though the simulation included all EPs with different momenta. This angle range is extracted from the k-width of the EP dispersion curve in the angle-resolved reflectance spectra, fitted by a Lorentzian function. All simulations averaged 120 independent runs.

For EP simulations of resonant excitation (Figure 3f), where the EP population can saturate within the pump pulse width, we additionally introduce EP-EP scattering. We estimate the scattering time using the semiclassical approximation¹⁰:

$$\tau_{scatter} = (\tau_{pol}^{-1} + \tau_{phonon}^{-1})^{-1}$$
$$\tau_{pol}^{-1} = \sigma n v$$

where σ is the EP scattering cross-section, n is the polariton density, and v is the group velocity. σ was calculated by $\sigma = \sigma_{EX}|X|^4$, where σ_{EX} is the exciton-exciton scattering cross-section (4 nm, assigned as the exciton Bohr radius¹¹).

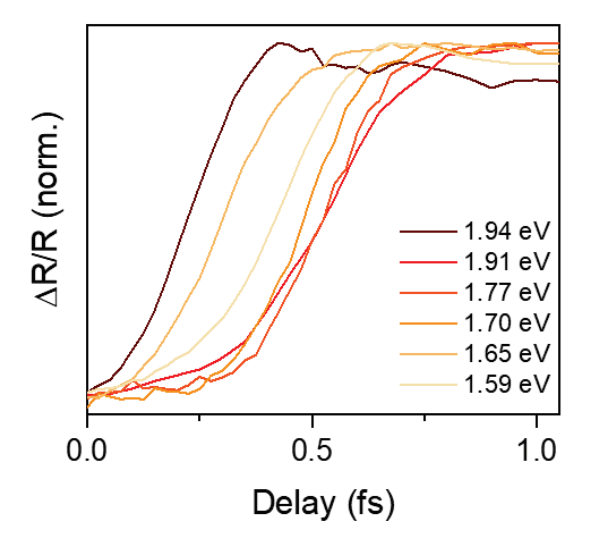


Figure S7. The temporal rise-time for EPs probed at different energies (corresponding to the data in Figure 2) following above-gap excitation.

To model the MUPI image formation process, the spatial EP population distribution is convolved with a filter function that models the interference between the widefield probe (plane wave) and spherical wave scattering from the EP population (Figure S8), i.e.:

$$\overrightarrow{E_{sp}} = \frac{A}{r} e^{i(k|\vec{r} - \overrightarrow{r_1}| - \omega t + \phi_1)}$$

$$\overrightarrow{E_p} = C e^{i(\vec{k}\vec{r} - \omega t + \phi_2)}$$

$$I = |\overrightarrow{E_{sp}} + \overrightarrow{E_p}|^2 = |\overrightarrow{E_{sp}}|^2 + |\overrightarrow{E_p}|^2 + 2\overrightarrow{E_{sp}} \cdot \overrightarrow{E_p} = \left(\frac{A}{r}\right)^2 + C^2 + 2\frac{AC}{r} cos[k(r - rcos\theta) + \Delta\phi]$$

Where I is the light intensity detected on the CMOS camera, A and C are the wave amplitudes, and k, ω are spatial angular frequency and circular frequency of the electromagnetic wave. \vec{k} is the wavevector, \vec{r} is the position vector, and θ represents the angle between the vectors. ϕ is an arbitrary phase tuned to match the experimental profile. The resulting images (shown in Figure 1e of the main text) for different time delays closely reproduces the characteristic MUPI profile of interference-like features near the pump excitation location, as well as a ballistically expanding wavefront along the probed wavevector.

All Monte-Carlo simulations were carried out in python.

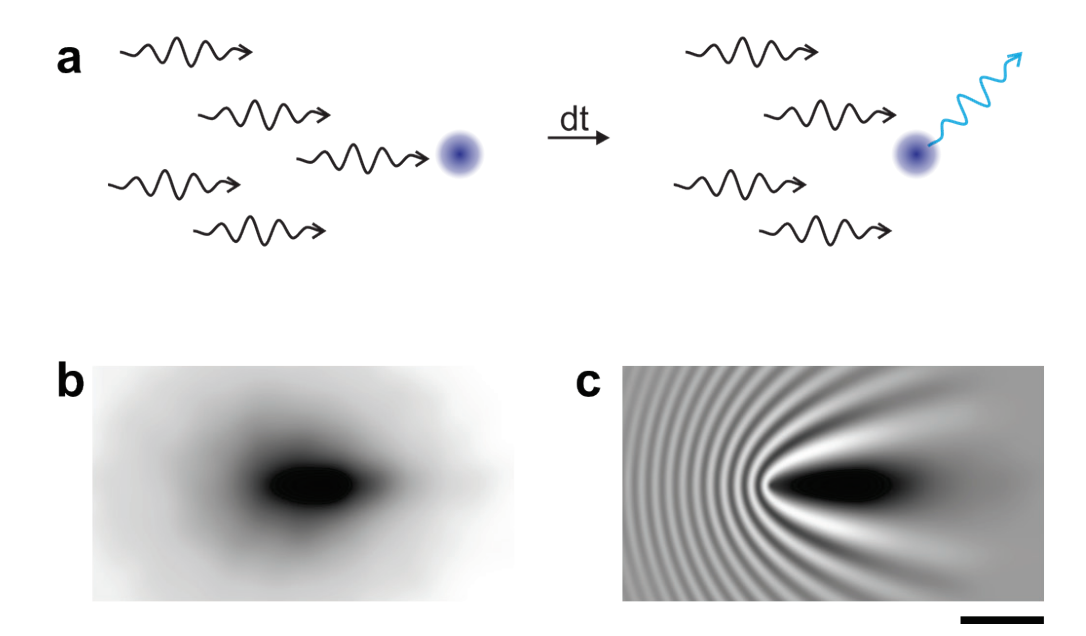


Figure S8. EP transport Monte-Carlo simulations. (a) Illustration of the time-stepping process in our simulations. (b) The spatial distribution of EPs as 'particles' in the Monte-Carlo simulations at a time delay of 400 fs, for EPs at 1.91 eV with a group velocity of 20.35 μ m/ps and a measured propagation speed of 15.3 μ m/ps. The black scale level represents EP density. (c) Same as panel (b) after convolution with the interference filter function. The scale bar is 2 μ m.

6. Simulations of ground and transient angle-resolved reflectance spectra

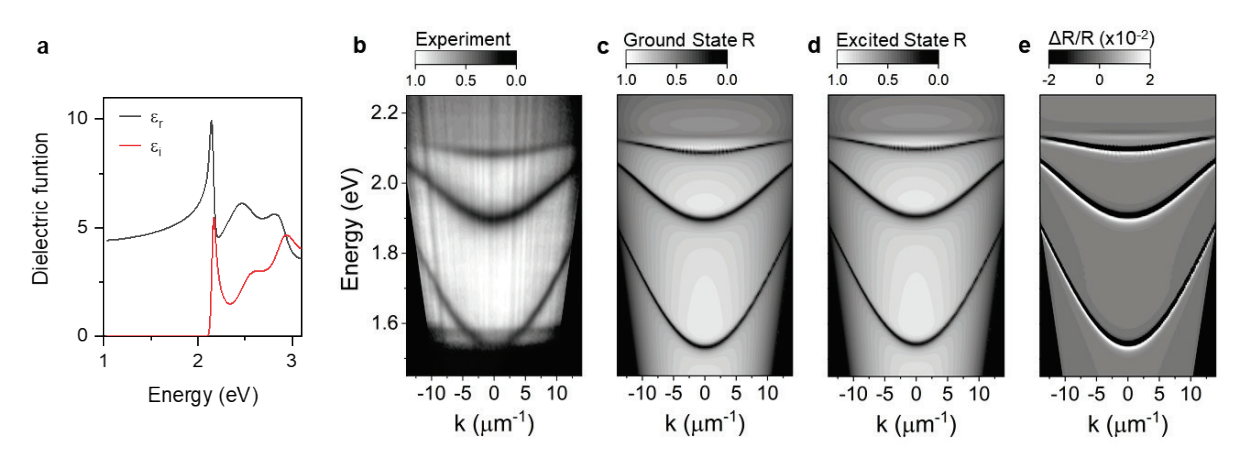


Figure S9. Simulated angle-resolved spectra. (a) The ground state dielectric function of BA₂(MA)Pb₂I₇.¹² (b) Momentum-resolved reflectance the Au/Perovskite/Ag cavity. (c) Simulated momentum-resolved reflectance spectra of the same cavity. (d) Simulated excited state reflectance spectra of the same cavity, using a blueshifted dielectric function for the 2D perovskite, and assuming 3% of oscillators are populated. (e) Transient reflectance spectra obtained by computing the differential reflectance from panel (c) and panel (d) (see text), corresponding to data presented in Figure 1i of the main text.

To simulate and analyze the angle-resolved reflectance profiles presented in Figures 1h-j of the main text, we turn to a scattering matrix approach, which we perform using the open-source S4 package. We first start by simulating the ground state (linear) angle-resolved reflectance profile. Input simulation parameters are the ground state dielectric function of BA₂(MA)Pb₂I₇ (figure S9a) which we obtain from the literature; incident light angle (varied from 0 to 90 degrees) and polarization (s-polarized); the cavity thickness (0.667 µm); and mirror layers (30 nm gold and 150 nm silver), with light incident through the gold. Figure 1h shows the resulting linear angle-resolved reflectance profile, which agrees well with the experimental data (Figure S9b).

The experimental transient angle-resolved reflectance profile (Figure 1i of the main text) displays a ~10 meV blueshift of all ground state polariton branches almost uniformly across all momenta. We hypothesize that this uniform blueshift arises due to a well-known pump-induced shift of the dielectric function in 2D halide perovskites. This pump-induced shift, typically on the order of 5-15 meV, 14 occurs due to excitonic many-body interactions.

To test our hypothesis, we used the scattering matrix approach to calculate the angle-resolved reflectance profile using the excited-state dielectric function of BA₂(MA)Pb₂I₇. Considering that not all excitons are populated, the excited state dielectric function is generated by averaging 3% of a 10 meV blueshifted dielectric with the ground state dielectric function. We then simulate the transient (differential) angle-resolved reflectance profile by calculating

$$\frac{\Delta R(\theta)}{R(\theta)} = \frac{R_{\text{excited}}(\theta) - R_{\text{ground}}(\theta)}{R_{\text{ground}}(\theta)}$$

Where R_{ground} (Figure S9c) and R_{excited} (Figure S9d) are generated with the ground-state (Figure S9a) and excited-state dielectric functions, respectively. As shown in Figure S9e, the simulated spectra agree closely with the experimental spectra (Figure 1i), suggesting that a simple exciton-induced dielectric-shift model is sufficient to explain the observed lower polariton blueshift for spatially overlapped pump/probe data. In other words, although the signal appears along the lower polariton branch dispersion, this signal reports on the exciton population rather than the EP population.

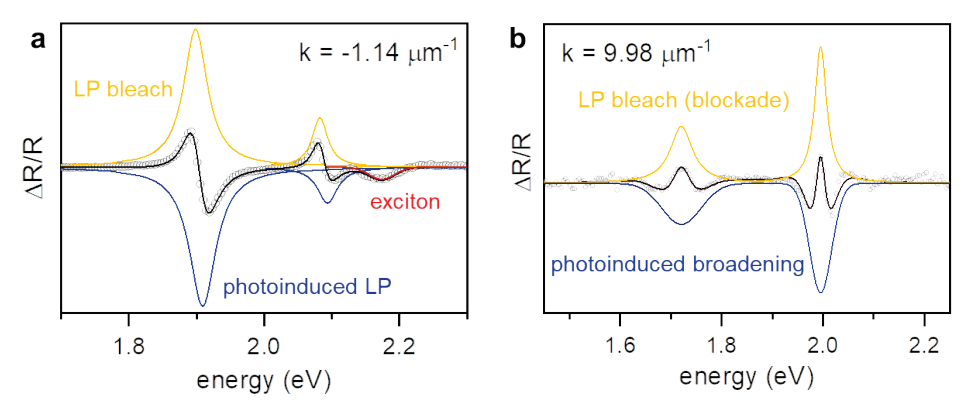


Figure S10. Spectral cuts from transient angle-resolved reflectance spectra for: (a) spatially-overlapped pump and probe pulses, and (b): spatially-separated (>1 μ m) pump and probe pulses. Data points are black circles. The black line represents the total fit, composed from adding the yellow, blue, and red (for the exciton resonance in panel a) fit components. Note that the spectral cuts are taken at different values of k for the spatially-overlapped (-1.14 μ m⁻¹) vs separated (9.98 μ m⁻¹) pump-probe data.

To further investigate the nature of the signal in both spatially-overlapped (Figure 1i) and spatially-separated (Figure 1j) pump-probe transient reflectance profiles, we analyze spectral line cuts at specific momenta in Figure S10. For the spatially overlapped data (Figure S10a), line cuts along any momentum (here shown for $k = -1.14 \ \mu m^{-1}$) provide an alternative visualization of the aforementioned dielectric blueshift simulated in Figure S9. The observed transient features are fit with two Lorentzian functions, where the positive component represents 'bleaching' of the lower polariton branch (disappearance of the lower polariton branch from its ground state energy, resulting in more reflectance), and the blueshifted negative component represents the new spectral location of the branch. The extra bump at 2.16 eV is from the exciton reservoir.

For spatially separated transient reflectance (Figure S10b), with pump probe separation distances exceeding 1 micron and at a time delay of 1 ps, the transient angle-resolved spectra must report on the EP population since excitons are immobile on this timescale. Here, the transient profiles look different: the most noticeable feature is a broadening of the polariton band. The net result is a bleach of the original polariton band (fit with a positive Lorentzian), signifying that probe photons with energies and momenta matching the ground state LP are not able to enter the cavity, and new photon pass-bands (fit with a negative Gaussian function) either side of the original polariton band, indicating that photons with slightly higher and lower energies are now able to enter the cavity and populate EPs. This behavior closely resembles a blockade-like effect¹⁵: when pump-populated EPs are present at a specific location in space, probe photons are unable to populate EPs at the exact

same energy and location. Such repulsive EP-EP interactions are known to lead to spectral broadening (imaginary self-energy)¹⁶, the main feature observed in Figure S10b.

These transient angle-resolved reflectance profiles thus indicate that the mechanism for contrast generation in MUPI arises from blockade-like EP-EP interactions, whereby the imaged probe field is modified by the presence of propagating pump-generated EPs: the latter change the probability for probe photons to enter the cavity at the center probe energies, resulting in enhanced or suppressed reflectivity depending on the exact probe energy and momentum selected.

7. Theory of EP-lattice scattering

I. Model Hamiltonian

We consider a simple one-dimensional model^{17,18} with both Peierls and Holstein-type excitonphonon interactions coupled to a set of radiation modes inside an optical cavity¹⁹. The light-matter Hamiltonian in atomic units ($\hbar = 1$) is given as ^{19–21},

$$\hat{H} = \sum_{n} (\epsilon_{0} + \gamma \hat{q}_{n}) \hat{c}_{n}^{\dagger} \hat{c}_{n} + \sum_{n} (\hat{c}_{n+1}^{\dagger} \hat{c}_{n} + \hat{c}_{n}^{\dagger} \hat{c}_{n+1}) [\alpha(\hat{q}_{n+1} - \hat{q}_{n}) - \tau] + \sum_{n} \frac{\hat{p}_{n}^{2}}{2m} + \frac{1}{2} K \hat{q}_{n}^{2} + \sum_{\mathbf{k}, n} \frac{g_{c}}{\sqrt{N}} \sqrt{\frac{\omega_{\mathbf{k}}}{\omega_{0}}} (\hat{\mu}_{n} \cdot \hat{\epsilon}_{\mathbf{k}}) (\hat{a}_{\mathbf{k}} e^{i\mathbf{k} \cdot X_{n}} + \hat{a}_{\mathbf{k}}^{\dagger} e^{-i\mathbf{k} \cdot X_{n}}) + \sum_{\mathbf{k}} \hat{a}_{\mathbf{k}}^{\dagger} \hat{a}_{\mathbf{k}} \omega_{\mathbf{k}} \tag{S1}$$

In the light-matter Hamiltonian expressed above, \hat{c}_n^{\dagger} and \hat{c}_n are the excitonic creation and annihilation operators at site n=1,2...N located at $X_n=n\cdot L$ with transition dipole $\hat{\mu}_n=\hat{x}(\hat{c}_n+\hat{c}_n^{\dagger}),\,\hat{a}_{\bf k}^{\dagger}$ and $\hat{a}_{\bf k}$ are the photonic creation and annihilation operators of cavity mode ${\bf k}$ with a frequency $\omega_{\bf k}$ and polarization direction $\hat{\epsilon}_{\bf k},\,\epsilon_0$ is the exciton site energy, $\{\hat{q}_n\}$ and $\{\hat{p}_n\}$ are the position and momentum operators of a set of phonon modes with frequency $\omega_{\bf p}=\sqrt{K/m}$ and m,γ and α characterizes local (Holstein) and non-local (Peierls) exciton-phonon coupling strengths, g_c is the exciton-photon coupling strength and τ is a hopping parameter. As in past work on halide perovskites $^{22-24}$, we treat the lattice classically. While this model can be studied on a two-dimensional lattice, we do not expect qualitative differences from the one-dimensional case we treat here.

For a two-dimensional cavity²⁰ with a confinement in the y direction with a length L_y , the transverse primary photon mode wavevector is $k_y = \pi/\eta_r L_y$ where η_r is the refractive index of the medium (assumed as 1 for simplicity). Assuming periodic boundary conditions in the x direction, such that $X_{N+1} \equiv X_1$, the cavity mode wavevectors in the x direction become $k_x = 0, \pm \frac{2\pi}{N \cdot L} \dots, \pm k_{\max}$, where we choose $k_{\max} = N_c \frac{2\pi}{N \cdot L}$ as a numerical cutoff to only include energetically relevant cavity modes. Thus, the set of cavity modes are $\mathbf{k} = \{(k_x, k_y)\} = \{(0, k_y), (\pm \frac{2\pi}{N \cdot L}, k_y), \dots, (\pm k_{\max}, k_y)\}$ with the corresponding photon frequencies $\omega_{\mathbf{k}} = c |\mathbf{k}| = c \sqrt{k_x^2 + k_y^2}$.

In this work, the light-matter Hamiltonian is represented in the single excited subspace $\{|e_n, 0\rangle, |g, 1_k\rangle\}$, where $|e_n, 0\rangle$ represents an excitation at site n and 0 photons in the cavity, and $|g, 1_k\rangle$ represents a photonic excitation on the \mathbf{k}^{th} mode with no excitation in the matter-subsystem. The light-matter Hamiltonian in the $\{|e_n, 0\rangle, |g, 1_k\rangle\}$ basis is given as

$$\begin{split} \widehat{H} &= \sum_{n} (\epsilon_{0} + \gamma \widehat{q}_{n}) |e_{n}, 0\rangle \langle e_{n}, 0| + \sum_{n} \frac{\widehat{p}_{n}^{2}}{2m} + \frac{1}{2} K \widehat{q}_{n}^{2} + \sum_{\mathbf{k}} \omega_{\mathbf{k}} |g, 1_{\mathbf{k}}\rangle \langle g, 1_{\mathbf{k}}| \\ &+ \sum_{n} [\alpha(\widehat{q}_{n+1} - \widehat{q}_{n}) - \tau] (|e_{n+1}, 0\rangle \langle e_{n}, 0| + |e_{n}, 0\rangle \langle e_{n+1}, 0|) \\ &+ \sum_{\mathbf{k}, n} \frac{g_{c}}{\sqrt{N}} \sqrt{\frac{\omega_{\mathbf{k}}}{\omega_{0}}} (\widehat{x} \cdot \widehat{\epsilon}_{\mathbf{k}}) (|e_{n}, 0\rangle \langle g, 1_{\mathbf{k}} | e^{i\mathbf{k}\cdot X_{n}} + |g, 1_{\mathbf{k}}\rangle \langle e_{n}, 0| e^{-i\mathbf{k}\cdot X_{n}}) \end{split}$$
(S2)

We emphasize that the exciton-phonon coupling only appears in the $\{|e_n,0\rangle\}$ subspace. This is why higher photonic character in a polariton state leads to lower effective polariton-phonon coupling. Below we tabulate the parameters used in this work which are adapted from Ref ^{18,25} and not to be taken as necessarily realistic for perovskite materials.

N	$N_{\rm c}$	ϵ_0	τ	α	γ	ω_0	m	K	g_c	L
6001	150	2.2	300	995	3000	1.7	150	14500	0.1	100
		eV	cm ⁻¹	cm ⁻¹ /Å	cm ⁻¹ /Å	eV	amu	amu/ps^2	eV	Å

I-a. Polariton Bands

We can obtain polariton bands analytically if we ignore the phonons. The bands are then obtained by solving the following 2×2 Hamiltonian^{26,27} (setting $\cos\theta_{\mathbf{k}} = \hat{x} \cdot \hat{\epsilon}_{\mathbf{k}}$),

$$\widehat{H}_k^0 = \begin{bmatrix} \epsilon_k & g_c \sqrt{\cos \theta_k} \\ g_c \sqrt{\cos \theta_k} & \omega_k \end{bmatrix}.$$

Here, $k \equiv k_x$ is used to label wavevectors instead of **k** for simplicity. The upper and lower polariton bands are then given as

$$E_{\pm}(k) = \frac{1}{2}(\epsilon_k + \omega_k) \pm \sqrt{(\epsilon_k - \omega_k)^2 + 4g_c^2 \cos\theta_k}.$$

The Rabi-splitting Ω_c when $\omega_k = \epsilon_k$ is $\Omega_c = 2g_c\sqrt{\cos\theta_k}$. In the model considered here $\epsilon_k = \epsilon_k - 2\tau \cdot \cos(k \cdot L)$. Further, ϵ_k can be replaced with $\epsilon_k \approx \epsilon_{k=0} = \epsilon_k - 2\tau = E_0$.

II. Quantum Dynamics Approach

In this work we employ a mixed quantum-classical approach to propagate quantum dynamics of the light-matter system. The phonon degrees of freedom (DOF) are treated classically while the electron-photon subsystem is treated quantum mechanically. The coupled motion of electronic and nuclear DOF are evolved using the mean-field Ehrenfest method.

II-a. Mean Field Ehrenfest Method

We treat the phonon DOF as nuclear degrees of freedom and evolve them classically. The photonic and excitonic DOF are evolved by solving the Time-Depended Schrödinger Equation (TDSE) for the "electronic" part (includes electronic and photonic DOF) of the Hamiltonian

$$\widehat{H}_{\text{el-ph}} = \widehat{H} - \sum_{n} \frac{\widehat{p}_n^2}{2m}.$$

More precisely, the electronic-photonic wavefunction $|\Psi(t)\rangle$ is defined as

$$|\Psi(t)\rangle = \sum_{i} c_{j}(t) |\Phi_{j}(\mathbf{q})\rangle,$$

where $|\Phi_j(\mathbf{q})\rangle$ are the polaritonic states, which are the eigenstates of \widehat{H}_{el-ph} , i.e. $\widehat{H}_{el-ph}|\Phi_j(\mathbf{q})\rangle = \mathcal{E}_j(\mathbf{q})|\Phi_j(\mathbf{q})\rangle$. Thus, during each nuclear step Δt the electronic-photonic wavefunction is evolved simply as

$$|\Psi(t+\Delta t)\rangle = \sum_{j} c_{j}(t) e^{i\varepsilon_{j}(\mathbf{x})\Delta t} |\Phi_{j}(\mathbf{q}(t))\rangle.$$

The nuclear DOF in this approach is evolved with nuclear force

$$F_n(t) = \sum_{ij} c_i^*(t) c_j(t) \langle \Phi_i(\mathbf{q}(t)) | \nabla_n \widehat{H}_{el-ph} | \Phi_j(\mathbf{q}(t)) \rangle.$$

In this work we have used a nuclear time-step of $\Delta t = 10$ fs to obtain converged dynamics.

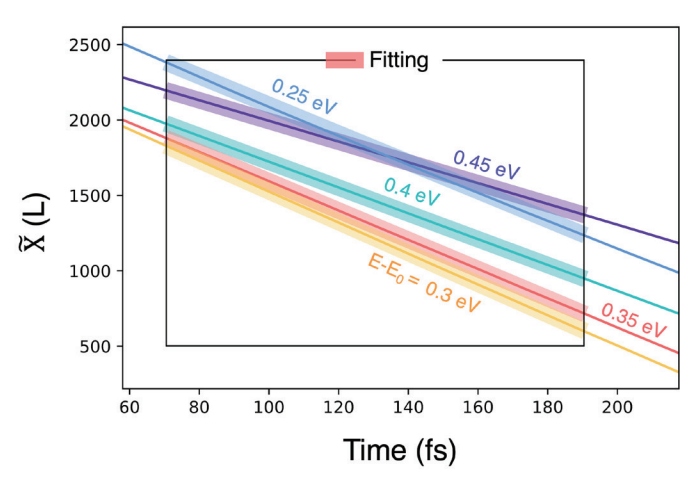


Figure S11. Calculating the group velocity from direct numerical simulations. Time-dependent wavefront position of the polaritonic wavepacket (solid line) initially prepared within distinct energy windows. Transparent lines indicate linear fits of the wavefront position.

II-b. Initial Conditions

We create an excitonically localized initial condition which is a linear combination of polaritonic states that lie in some specified energy window, $\left[E - \frac{\Delta E}{2}, E + \frac{\Delta E}{2}\right]$. That is

$$|\Psi(0)\rangle = \sum_{i} c_{j}(0) |\Phi_{j}(\mathbf{q})\rangle,$$

where the index j denotes the inclusion of states such that the condition $E - \frac{\Delta E}{2} \le \mathcal{E}_j(\mathbf{x}) \le E + \frac{\Delta E}{2}$ is satisfied. In this work we use $\Delta E = 0.025$ eV. The coefficients, $\{c_j(0)\}$ are obtained through a Monte Carlo procedure which maximizes excitonic localization by minimizing

$$\Delta X^2 = \sum_n \rho_n X_n^2 - \left(\sum_n \rho_n X_n\right)^2,$$

where $\rho_n = |\langle e_n, 0 | \Psi(0) \rangle|^2 / \sum_m |\langle e_m, 0 | \Psi(0) \rangle|^2$.

The phonon DOFs are sampled from a classical Boltzmann distribution,

$$\rho(q_n,p_n) \propto e^{-\beta \left(\frac{\widehat{p}_n^2}{2m} + \frac{1}{2}K\widehat{q}_n^2\right)},$$

where $\beta = 1/k_BT$ (T = 300K). In this work we have used 250 trajectories to converge all results.

III. Numerical Details

To extract the velocities of wavefronts from our simulations, we compute the position of the wavefront $\tilde{X}(t) = L \cdot N'$ where N' is determined from is obtained by solving from the expression

$$\sum_{n=0}^{N'} \rho_n = P_X$$

where $\rho_n = |\langle e_n, 0|\Psi(0)\rangle|^2 / \sum_m |\langle e_m, 0|\Psi(0)\rangle|^2$, and $P_X = 0.05$ is chosen to define the position of the wavefront such that 5% of excitonic probability has crossed $\tilde{X}(t)$ at time t. The velocity of the wavefront is then computed by fitting $\tilde{X}(t)$.

Figure S11 presents the time-dependent wavefront position of the polaritonic wavepacket initially prepared within various energy windows. We obtain group velocities by linearly fitting between 72-188 fs. These group velocities are reported in the main text. These simulations were done using the Extreme Science and Engineering Discovery Environment (XSEDE)²⁸ and specifically Open Science Grid Consortium.^{29,30}

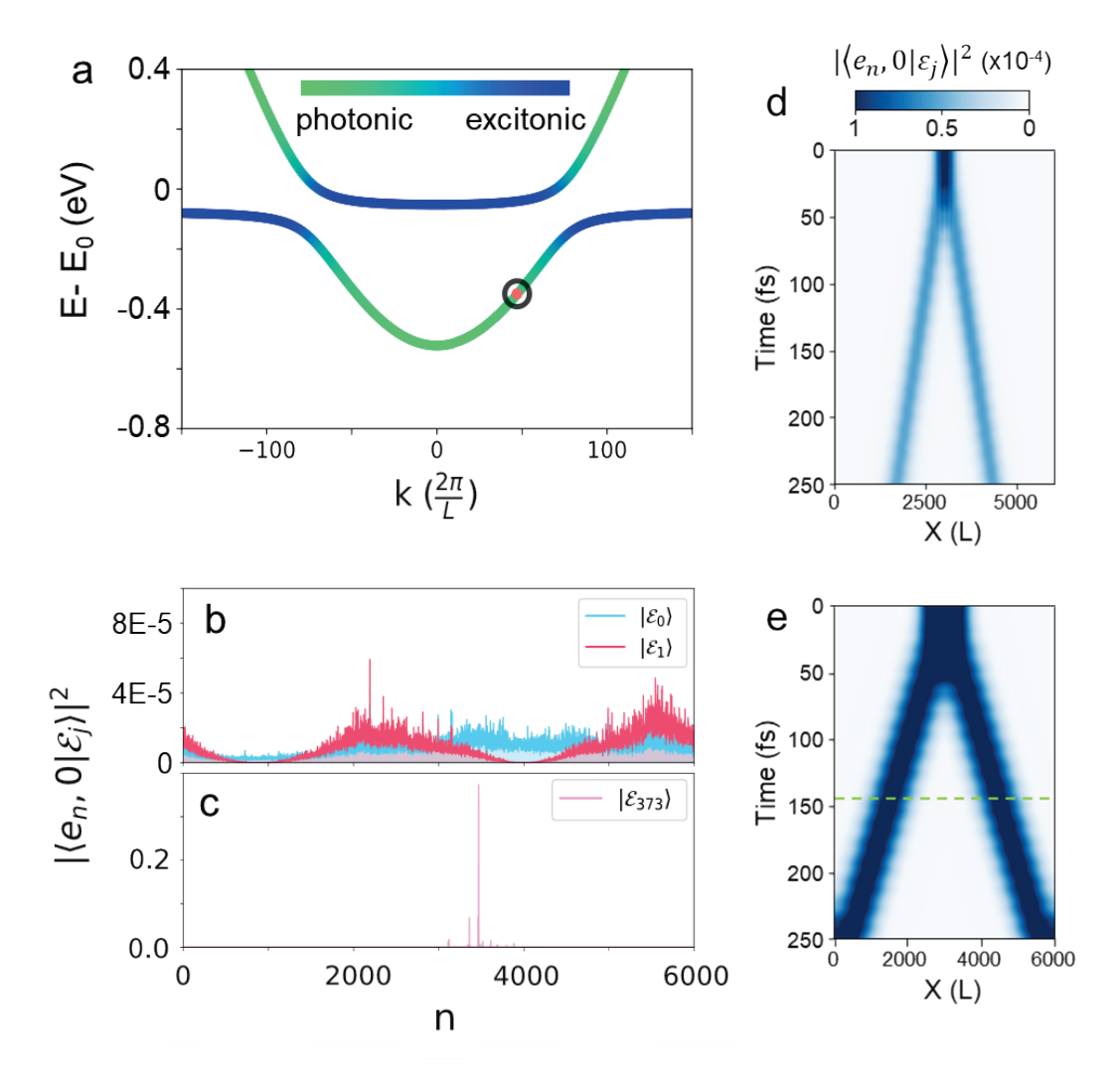


Figure S12. Quantum dynamical simulation of exciton-polariton motion. (a) Polaritonic bands (ignoring phonons) with color coding that represent the excitation character. (b) Polaritonic eigenstates $|\mathcal{E}_0\rangle$ and $|\mathcal{E}_1\rangle$ (5% excitonic character) that are delocalized in site (position) space. (c) Polaritonic eigenstate $|\mathcal{E}_{371}\rangle$ that lies around $\approx E_0 - 0.1$ eV (98% excitonic) which is localized in site space. (d) Ballistic spreading of the polaritonic probability density ("light-cone") as a function of site location, starting with a localized initial wave-packet with an energy-window centered at E-E_{ex} = 0.475 ± 0.025 eV, circled in (a). (e) Ballistic spreading of polaritonic probability density for the same detuning as in Figure 2d of the main text, but with lower exciton-phonon coupling (setting γ = 0). The wave front of the polariton wave-packet propagates always ahead of the one with phonon scattering. The green dash line cuts at 145 fs is plotted in figure 2e.

8. Additional data and fits for EP propagation under non-resonant and resonant excitation

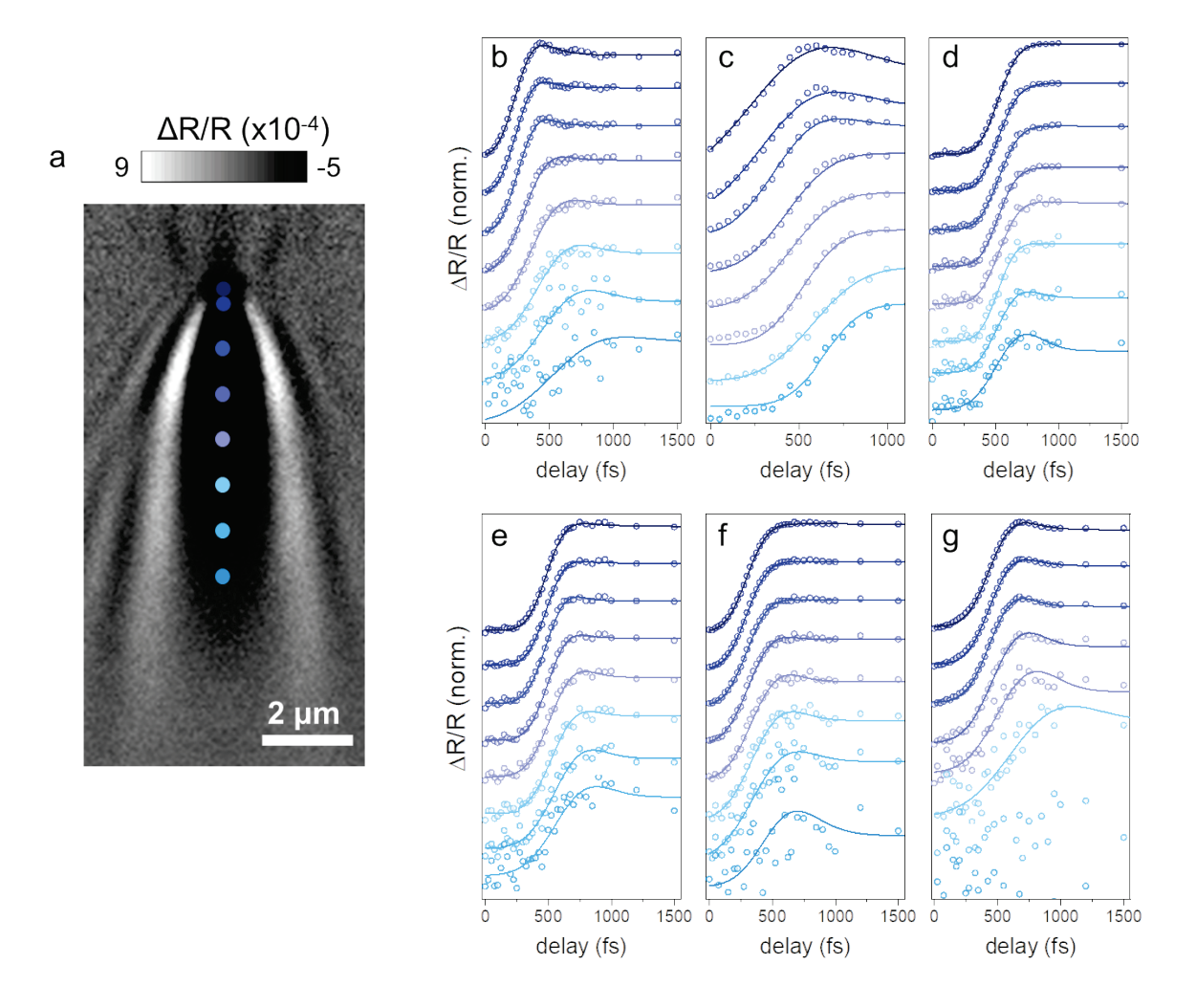


Figure S13. Fitting of propagation data for Figure 2 of the main text. (a) Blue dots represent spatial locations for which we fit the signal grow-in time to extract the polariton propagation velocity. From bottom to top, the distances are 0, 0.32, 1.33, 2.35, 3.37, 4.32, 5.33, and 6.35 μm away from excitation location. Scale bar is 2 μm. (b-g) Temporal profiles used to extract propagating speed. The distance increases from top to bottom. Lines are fits using a Gaussian function convolved with an exponential decay. From (b) to (g), the EP energies are 1.94 eV, 1.91 eV, 1.77 eV, 1.70 eV, 1.65 eV and 1.59 eV, respectively. The 1.59 eV EP showed relatively short propagation, so the last two position do not display any grow-in. Pump fluence is 5.75 μJ/cm².

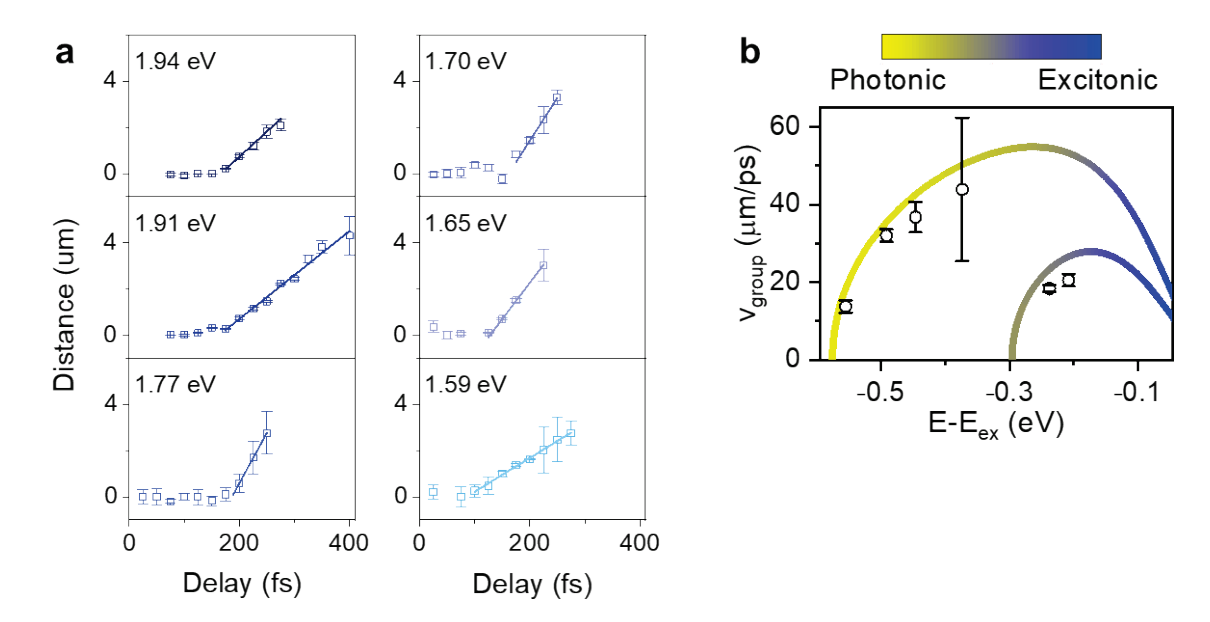


Figure S14. (a) Additional examples for time-resolved EP propagation following resonant pump excitation (complementary data to Figure 3f). The initial apparently immobile signal is assigned to EP-EP scattering following resonant excitation, which creates a dense population of EPs within the pump pulse temporal width of ~60 fs. In Figure 3f of the main text, we show Monte-Carlo simulations that reproduce this behavior. (b) Extracted measured EP velocities compared to the expected group velocities for resonant pump excitation, showing almost identical behavior to non-resonant excitation data in Figure 2b.

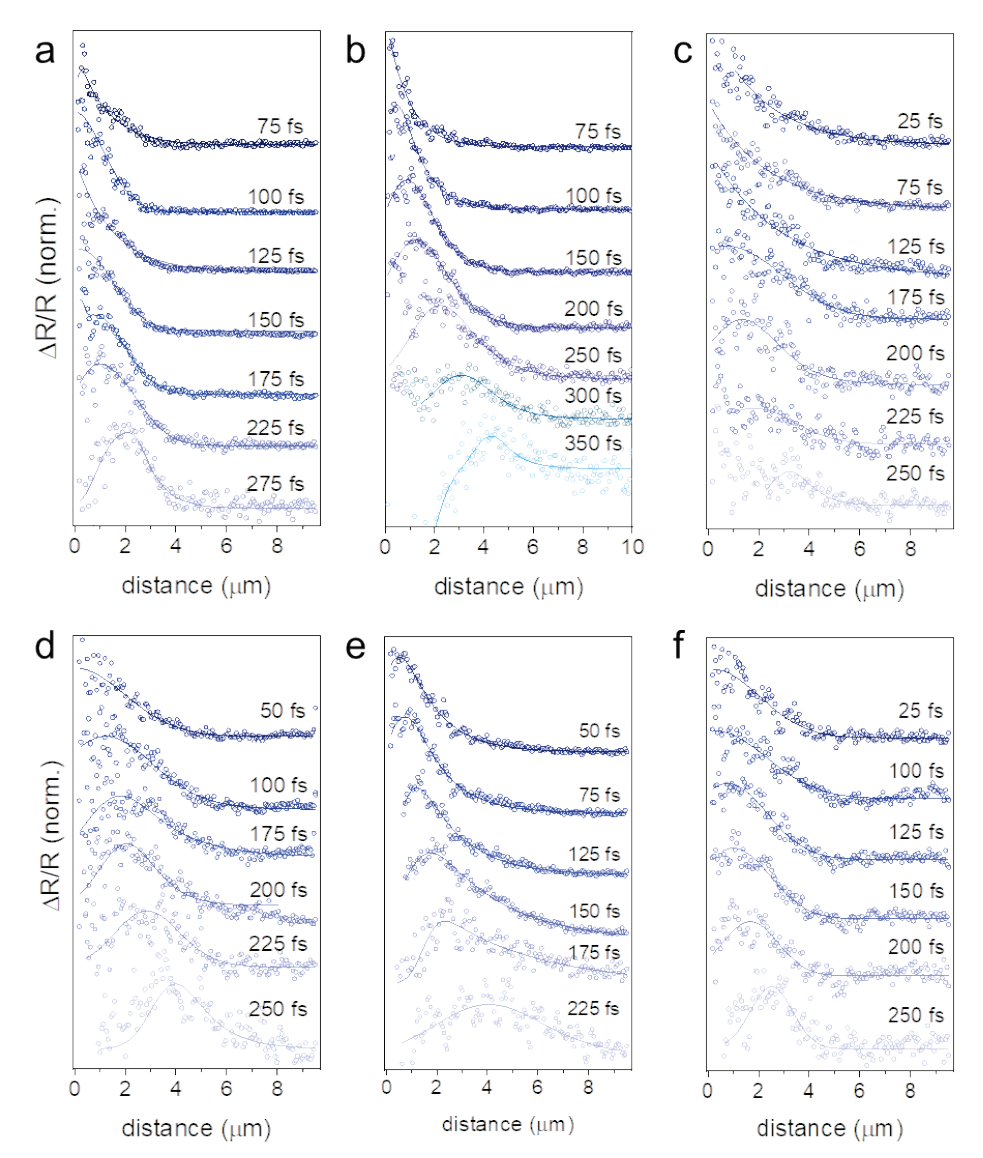


Figure S15. Data fits for the resonant excitation EP propagation data presented in Figure S14. (a-f) Temporal evolution series for EP energies of 1.94 eV, 1.91 eV, 1.77 eV, 1.70 eV, 1.65 eV and 1.59 eV, respectively. Note that for resonant excitation, a clear wavepacket-like feature is observed because there are no reservoir exciton states refilling the LP branch and causing the elongated features observed in non-resonant excitation. As such, fitting for resonant excitation experiments is performed by tracking the position of the maximum amplitude of the wavepacket, as illustrated in the figure.

9. Characterization of cavity-free polaritonic slabs

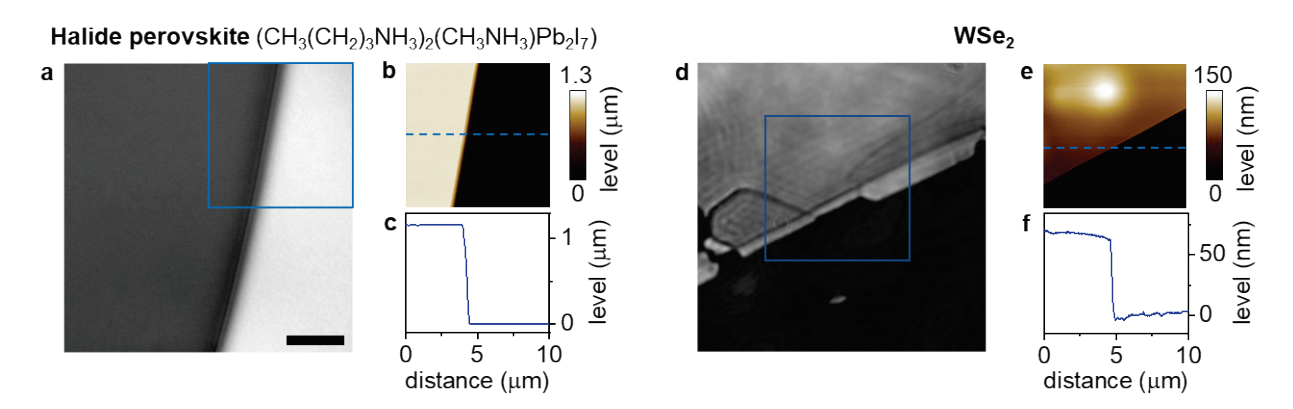


Figure S16. Optical images (a,d), atomic force microscopy images (b, e) and corresponding line cuts (c, f) for the layered halide perovskite and WSe₂ slabs used for Figures 4b and 4c. The layered perovskite slab is 1.13 µm thick. The WSe₂ slab is 69 nm thick.

References

- 1. Ruddlesden, S. N. & Popper, P. The compound Sr₃Ti₂O₇ and its structure. *Acta Crystallogr.* **11**, 54–55 (1958).
- 2. Stoumpos, C. C. *et al.* Ruddlesden-Popper Hybrid Lead Iodide Perovskite 2D Homologous Semiconductors. *Chem. Mater.* **28**, 2852–2867 (2016).
- 3. Edelberg, D. *et al.* Approaching the Intrinsic Limit in Transition Metal Diselenides via Point Defect Control. *Nano Lett.* **19**, 4371–4379 (2019).
- 4. Tang, Y. *et al.* Simulation of Hubbard model physics in WSe₂/WS₂ moiré superlattices. *Nature* **579**, 353–358 (2020).
- 5. Pau, S., Björk, G., Jacobson, J., Cao, H. & Yamamoto, Y. Microcavity exciton-polariton splitting in the linear regime. *Phys. Rev. B* **51**, 14437–14447 (1995).
- 6. Su, R. *et al.* Observation of exciton polariton condensation in a perovskite lattice at room temperature. *Nat. Phys.* **16**, 301–306 (2020).
- 7. Ginsberg, N. S. & Tisdale, W. A. Spatially Resolved Exciton and Charge Transport in Emerging Semiconductors. *Annu. Rev. Phys. Chem.* **71**, 1–30 (2020).
- 8. Zhu, T., Snaider, J. M., Yuan, L. & Huang, L. Ultrafast Dynamic Microscopy of Carrier and Exciton Transport. *Annu. Rev. Phys. Chem.* **70**, 219–244 (2019).
- 9. Seitz, M. *et al.* Exciton diffusion in two-dimensional metal-halide perovskites. *Nat. Commun.* **11**, 2035 (2020).
- 10. Sun, Y. *et al.* Direct measurement of polariton–polariton interaction strength. *Nat. Phys.* **13**, 870–875 (2017).

- 11. Cheng, B. *et al.* Extremely reduced dielectric confinement in two-dimensional hybrid perovskites with large polar organics. *Commun. Phys.* **1**, 80 (2018).
- 12. Song, B. *et al.* Determination of Dielectric Functions and Exciton Oscillator Strength of Two-Dimensional Hybrid Perovskites. *ACS Mater. Lett.* **3**, 148–159 (2021).
- 13. Liu, V. & Fan, S. S4: A free electromagnetic solver for layered periodic structures. *Comput. Phys. Commun.* **183**, 2233–2244 (2012).
- 14. Wu, X., Trinh, M. T. & Zhu, X. Y. Excitonic Many-Body Interactions in Two-Dimensional Lead Iodide Perovskite Quantum Wells. *J. Phys. Chem. C* **119**, 14714–14721 (2015).
- 15. Fulton, T. A. & Dolan, G. J. Observation of single-electron charging effects in small tunnel junctions. *Phys. Rev. Lett.* **59**, 109–112 (1987).
- 16. Sun, Y. *et al.* Direct measurement of polariton-polariton interaction strength. *Nat. Phys.* **13**, 870–875 (2017).
- 17. Su, W. P., Schrieffer, J. R. & Heeger, A. J. Solitons in Polyacetylene. *Phys. Rev. Lett.* **42**, 1698–1701 (1979).
- 18. Wang, L., Beljonne, D., Chen, L. & Shi, Q. Mixed quantum-classical simulations of charge transport in organic materials: Numerical benchmark of the Su-Schrieffer-Heeger model. *J. Chem. Phys.* **134**, 244116 (2011).
- 19. Li, J. *et al.* Electromagnetic coupling in tight-binding models for strongly correlated light and matter. *Phys. Rev. B* **101**, 205140 (2020).
- 20. Tichauer, R. H., Feist, J. & Groenhof, G. Multi-scale dynamics simulations of molecular polaritons: The effect of multiple cavity modes on polariton relaxation. *J. Chem. Phys.* **154**, 104112 (2021).
- 21. Arnardottir, K. B., Moilanen, A. J., Strashko, A., Törmä, P. & Keeling, J. Multimode Organic Polariton Lasing. *Phys. Rev. Lett.* **125**, 233603 (2020).
- 22. Mayers, M. Z., Tan, L. Z., Egger, D. A., Rappe, A. M. & Reichman, D. R. How Lattice and Charge Fluctuations Control Carrier Dynamics in Halide Perovskites. *Nano Lett.* **18**, 8041–8046 (2018).
- 23. Schilcher, M. J. *et al.* The Significance of Polarons and Dynamic Disorder in Halide Perovskites. *ACS Energy Lett.* **6**, 2162–2173 (2021).
- 24. Lacroix, A., de Laissardière, G. T., Quémerais, P., Julien, J.-P. & Mayou, D. Modeling of Electronic Mobilities in Halide Perovskites: Adiabatic Quantum Localization Scenario. *Phys. Rev. Lett.* **124**, 196601 (2020).
- 25. Troisi, A. & Orlandi, G. Charge-Transport Regime of Crystalline Organic Semiconductors: Diffusion Limited by Thermal Off-Diagonal Electronic Disorder. *Phys. Rev. Lett.* **96**, 086601 (2006).
- 26. Michetti, P. & La Rocca, G. C. Polariton states in disordered organic microcavities. *Phys. Rev. B* **71**, 115320 (2005).

- 27. Keeling, J. & Kéna-Cohen, S. Bose-einstein condensation of exciton-polaritons in organic microcavities. *Annu. Rev. Phys. Chem.* **71**, 435–459 (2020).
- 28. Towns, J. et al. XSEDE: Accelerating Scientific Discovery. Comput. Sci. Eng. 16, 62–74 (2014).
- 29. Pordes, R. et al. The open science grid. J. Phys. Conf. Ser. 78, 012057 (2007).
- 30. Sfiligoi, I. *et al.* The pilot way to Grid resources using glideinWMS. in *2009 WRI World Congress on Computer Science and Information Engineering, CSIE 2009* vol. 2 428–432 (IEEE, 2009).